

Università degli Studi di Milano-Bicocca

Dipartimento di Scienze dell'Ambiente e della Terra

Corso di Laurea Triennale



*Statistical Cross-Validation of SWOT Altimetry-Derived Currents
Using In Situ Measurements from the BioSWOT-Med Campaign in the
Northwestern Mediterranean*

*Validazione statistica delle correnti derivate dall'altimetria SWOT
utilizzando misurazioni in situ dalla campagna BioSWOT-Med nel
Mediterraneo nord-occidentale*

Relatore:
Prof.ssa Claudia Pasquero

Candidato:
Antonio Favaloro

Correlatore:
Prof. Andrea Doglioli

ANNO ACCADEMICO 2024/2025

In mari via tua est.

Table of Contents

1. Introduction	5
1.1 Context and Motivation.....	5
1.1.1 Brief Overview of Oceanographic Observation Needs	5
1.1.2 Oceanographic Data Acquisition.....	6
1.2 Research Aims and Objectives	10
1.2.1 Cross-validating SWOT altimetry with in situ measurements	10
1.2.2 Research questions	11
2. Theoretical Background	12
2.1 Satellite Altimetry Basics.....	12
2.1.1 Altimetric Principles and Definitions (SSH, SLA, ADT)	12
2.1.2 Challenges: Accuracy, Coastal Contamination, Instrumental Noise.....	14
2.2 Geostrophic Velocity Theory.....	15
2.2.1 Fundamental Equations	15
2.2.2 Practical Computation (From SSH Gradients to Surface Velocity).....	18
2.2.3 Approximations and Reliability at Smaller Scales	18
2.3 Fine-Scale Oceanographic Structures	20
2.3.1 Fronts, Eddies, and Submesoscale Perturbations: Definitions	20
2.3.2 Observational Evidence (Vertical Profiles, Surface Patterns).....	21
2.4 Spectral Analysis and its Role in Oceanography	22
2.4.1 Spectral Analysis Fundamentals.....	22
2.4.2 Why Spectral Analyses Are Relevant for Identifying Oceanic Features	23
3. Missions and Campaigns	25
3.1 SWOT Mission	25
3.1.1 Historical Perspective of Satellite Altimetry and the “Revolution” of SWOT	25
3.1.2 Measurement Principles, Coverage, and Data Products	26
3.1.3 Strengths and Constraints of SWOT in Coastal/Submesoscale Areas	27
3.1.4 Role of MIO and Other Partners in Data Collection	27
3.2 BioSWOT-Med Campaign.....	28
3.2.1 General Presentation of the Field Campaign	28
3.2.2 Moving Vessel Profile (MVP).....	29
4. Methods: Data Processing & Statistical Approaches.....	31
4.1 Physical computation and data processing.....	31
4.1.1 Data Importation and Setup of Utility Functions	31
4.1.2 Loading and Filtering of Altimetric and In Situ Data	31
4.1.3 Interpolation on a Regular Grid and Smoothing	32
4.1.4 Calculation of Dynamic Height and Geostrophic Velocities	32
4.1.5 Generation of Output Graphs	34
4.2 Aggregated Sensitivity Analysis.....	35
4.2.1 Methodology and Physical Rationale	35
4.2.2 Implications of Cross-Validation and Calibration.....	36
4.3 Scatterplot Comparisons & Statistical Summaries	36
4.3.1 Selection and Interpretation of Statistical Metrics for Cal/Val	36
4.4 Spectral & Coherence Analysis	37
4.4.1 PSD Estimation and Ensemble Averaging	37
4.4.2 Coherence Computation and Technical Challenges.....	38

5. Results and Discussion	40
5.1 ADT Comparison and Velocity Fields	40
5.1.1 Graphical Presentation of ADT and Velocity Fields	40
5.1.2 Integrated Discussion and Comparative Analysis	44
5.2 Sensitivity Analysis	45
5.2.1 Graphical Presentation of the Aggregated Sensitivity Analysis	45
5.2.2 Integrated Discussion: Implications for Reference-Level Selection	46
5.3 Statistics	47
5.3.1 Presentation of Scatterplots and Statistical Summaries	47
5.3.2 Discussion: Statistical Insights and Relevance to the Study	49
5.4 Spectral Analysis	50
5.4.1 Concise Presentation of the Ensemble PSD and Coherence Plot	50
5.4.2 In-Depth Analysis: Scale Dependence, Ranking of PSD Curves, and Coherence Patterns	51
6. Final Conclusions and Outlook	52
6.1 Synopsis of Research	52
6.2 Limitations and Recommendations	53
6.3 Concluding Remarks	53
7. References	55
7.1 Figures References	58

1. Introduction

1.1 Context and Motivation

1.1.1 Brief Overview of Oceanographic Observation Needs

Oceanography is regarded as an interdisciplinary science, representing an effective approach to comprehending the interactions and processes of the complex system that is the ocean. Physical, chemical, biological, and geological processes interact with each other across different spatial and temporal scales, often resulting in non-linear systems and thus complex to model (Doe et al., 2018).

First, understanding oceanographic observations helps one to appreciate the complexity of the biogeophysical processes characterizing the marine environment (Smith et al., 2019). Covering more than 70% of the Earth, the oceans are essential for biogeochemical cycles, regulation of climate, and preservation of biodiversity (Vignudelli et al., 2019). The necessity for large-scale, temporally continuous data has grown even more critical given the rise of climate change and anthropogenic pressures such as pollution, overfishing, and coastal infrastructure.

With consequences for both science and society, these cases highlight some of the main topics of study and interest in oceanography:

- **Climate change and biogeochemical cycles:** The oceans represent the largest active carbon reservoir on Earth, given the yearly absorption of notable volumes of carbon dioxide (CO₂) from the atmosphere (Smith et al., 2019). Their contribution to the change of the greenhouse effect is complex since surface warming and deep mixing influence the capacity to absorb greenhouse gases (Doe et al., 2018). Besides, the oceans absorb heat from the atmosphere and disperse energy using current systems. Monitoring variations in temperature, salinity, organic and inorganic carbon content helps one to understand and project changes in climate throughout time spans from seasons to decades (Vignudelli et al., 2019).
- **Extreme climatic events:** The exchanges of heat and humidity between the ocean and the atmosphere will determine the development of cyclonic and anticyclonic systems capable of producing storms, typhoons, and hurricanes (Smith et al., 2020). Given the likelihood of such catastrophic events, especially in tropical and subtropical climates where sea surface temperature (SST) is relatively large, regular surveillance is necessary (Garcia & Wu, 2020).
- **Fisheries:** Most fish populations and aquaculture are determined by the condition of marine ecosystems, surface and deep currents that distribute nutrients, and the occurrence of upwelling zones (Martinez et al., 2018). Combining knowledge on nutrients, phytoplankton, and zooplankton with data on physicochemical qualities (pH, dissolved oxygen) helps plan economic activities including marine farming and fishing.
- **Coastal engineering:** Among the major difficulties in coastal engineering are sea-level rise, storm frequency fluctuations, and coastal erosion (Lee et al., 2018). Combining data on wave velocity, coastal currents, sediment deposition, and level variations enables one to assess mitigation strategies and adaptation (Martinez et al., 2018).
- **Ecology and Biodiversity:** Variations in temperature, pH, oxygen, salinity, and nutrient concentration define ecosystem dynamics and distribution of marine species (Brown et al., 2021). Supported by data, biological oceanography studies help to identify places of conservation value, assess how ocean acidification affects coral reefs, and track invading species (Roberts & Evans, 2019).

1.1.2 Oceanographic Data Acquisition

Scientific progress in the study of the oceans has also been made possible by the relentless technological development of oceanographic research instruments (Kim & Brown, 2021). These can be broadly divided into direct and indirect analytical tools. Direct data involves the collection and analysis of physical samples in situ (e.g. water or organisms), while indirect data uses remote sensing instruments and techniques to measure parameters without taking samples (Garcia & Wu, 2020). In situ instruments offer high vertical resolution measurements, providing insight into the evolution of physical and chemical parameters along the water column, at the expense of the reduced spatial coverage. On the other hand, remote sensing allows synoptic measurements of large parts of the ocean surface (satellite) or bottom (eco beamer) with a trade-off in vertical resolution (Smith, 2018). The combination of direct and indirect data is therefore advantageous.

1.1.2.1 In situ observations

In situ observations cover all measurements made directly in touch with water, the atmosphere, and marine life (Anderson et al., 2015). Their foundation is a broad spectrum of equipment and sampling techniques:

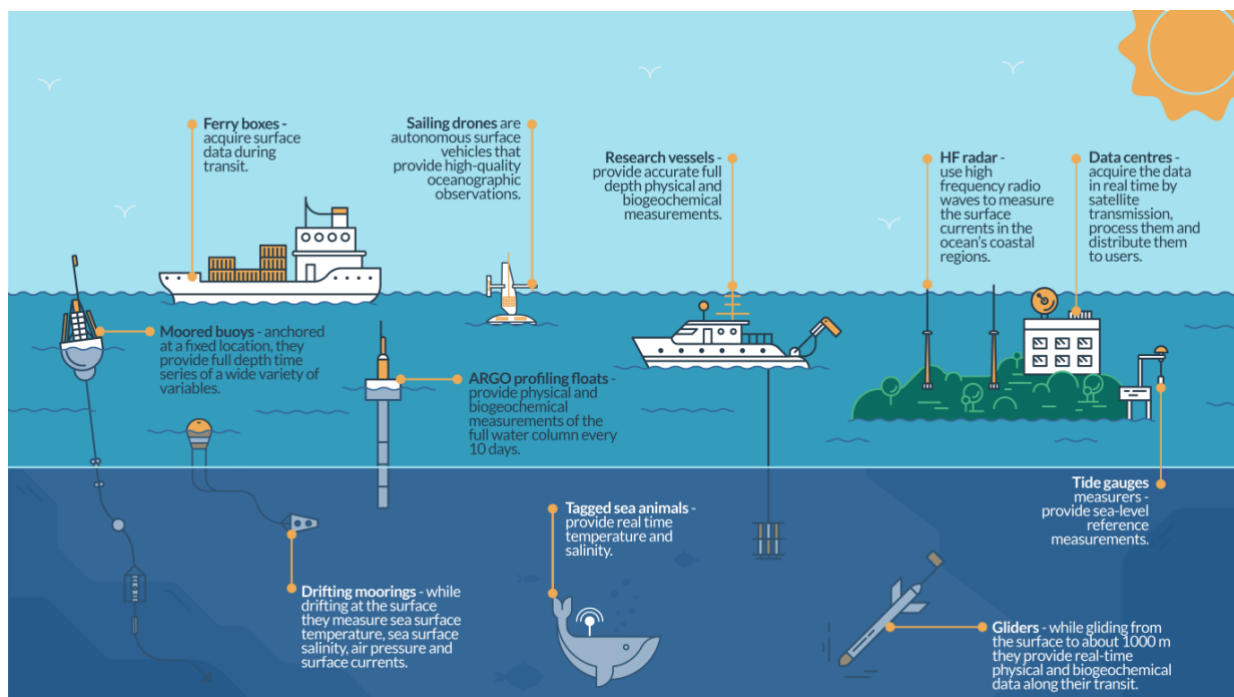


Figure 1. In situ observation platforms used for operational ocean monitoring.
Source: Copernicus Marine Service [1]

Research vessels let hydrographic and biological surveys along pre-defined paths with the possibility of always calibrating the instruments (CTD, Niskin bottles, plankton nets), gathering samples of water, sediments, and organisms, and measuring parameters including temperature, salinity, dissolved oxygen, chlorophyll, and nutrient concentration (Foster et al., 2017).

Moored buoys and drifting moorings can record meteorological data, physicochemical characteristics, and send them to processing facilities (Lee et al., 2018). Whereas drifters follow surface currents, fixed buoys offer long-term time series at designated places (Anderson et al., 2015).

Autonomous devices such as floats and gliders travel vertically in the water column gathering profiles of temperature, salinity, and occasionally oxygen and pH (Zhang et al., 2016). Particularly the Argo floats have shown to be essential in filling in knowledge gaps in far-off areas.

Tethered or autonomous robots allowing high spatial resolution measurements and targeted sampling in challenging or deep environments, including ocean trenches or polar areas, are ROV (Remotely Operated Vehicle) and AUV (Autonomous Underwater Vehicle).

The main benefits of in situ measurements are their accuracy and the ability of gathering physical samples for further in-depth analysis (such as chemical, genetic, and isotopic studies), as well as the direct instrument calibration (Anderson et al., 2015). The limitations, however, center on the limited spatial coverage since the missions are expensive in terms of financial and logistical resources as well as the likely impossibility of operating in bad weather conditions (Lee et al., 2018).

1.1.2.2 Remote sensing

Each technique of oceanic remote sensing is intended to measure distinct physical, chemical, and biological factors (Garcia & Wu, 2020). These techniques include bathymetric measurements, which map the depth and contour of the bottom, to approaches tracking ocean surface variables like temperature, salinity, and biological production. Among the several techniques, two of the most often used and powerful instruments are indirect acoustic or radar observations and satellite-based remote sensing (Hernandez et al., 2017).

The functioning of satellite remote sensing is enabled by:

- **Radiometric sensors**—those running in microwaves, visible light, and infrared—which offer data on sea surface temperature (SST), ocean color (from which chlorophyll concentration and primary production can be deduced), and sea ice coverage (Smith, 2018).




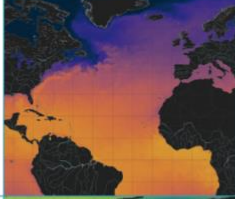


Type of instrument	What does it do	Examples of output	Variables that can be measured
	Spectroradiometer A spectroradiometer is a light measurement tool that is able to measure both the wavelength and amplitude of the light emitted from a light source. It can thus monitor the Earth's atmosphere, ocean and land surface in a wide wavelength spectrum ranging from the visible to near-infrared, medium-infrared and thermal frequencies. Outputs for the ocean include chlorophyll content, mineral and organic content, sea surface temperature and sea ice cover.		<ul style="list-style-type: none"> Chlorophyll content Organic and mineral content Sea surface temperature (SST) Sea ice cover
	Infrared radiometers Infrared radiometers are sensors that use infrared light to measure the radiation being reflected by surfaces and thus estimate the temperature of a surface without touching it. Outputs for the ocean are the sea surface temperature.		<ul style="list-style-type: none"> Sea surface temperature (SST)
	Microwave radiometer A microwave radiometer is a radiometer that measures energy emitted at millimetre-to-centimetre wavelengths, known as microwaves. They are very sensitive receivers designed to measure vertical profiles of important meteorological quantities, such as vertical temperature and humidity profile, columnar water vapor amount, or columnar liquid water. Outputs for the ocean include atmospheric water content (vapour and liquid), rain rates, sea ice concentration, sea surface temperature and salinity.		<ul style="list-style-type: none"> Atmospheric water vapour content Atmospheric water liquid content Rain rates Sea ice concentration Sea surface temperature (SST) Salinity

Figure 2. Satellite remote sensing instruments used in ocean monitoring and their measurable variables.
Source: Copernicus Marine Service [2]

- **Altimeters** measure millimetric fluctuations in sea level and enable the development of worldwide maps of the surface circulation field, therefore they're essential for the study of major currents (Gulf Stream, Kuroshio) or events like El Niño and La Niña (Davis et al., 2020).

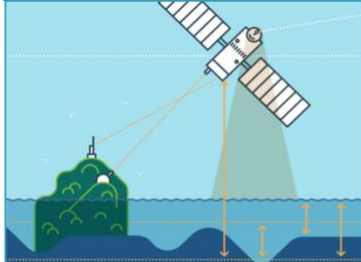

Type of instrument	What does it do	Examples of output	Variables that can be measured
	<p>Satellite altimeters</p> <p>Satellite altimeters are instruments that can make a global measurement of the surface topography. A satellite altimeter measures how long it takes for a short electromagnetic pulse sent from the satellite to reach the surface of the Earth surface and come back after being reflected by the surface. Outputs for the ocean include sea surface height, ocean surface wind speed, wave height and sea ice.</p>		<ul style="list-style-type: none"> Sea surface height Ocean surface wind speed Wave height Sea ice

Figure 3. Satellite altimeters used to measure sea surface height, wind speed, wave height, and sea ice conditions.
Source: Copernicus Marine Service [2]

- **Synthetic aperture radar (SAR)** enables the study of waves, surface currents, and pollution dispersion, enabling the detection of high resolution surface structures (Hernandez et al., 2017).



Type of instrument	What does it do	Examples of output	Variables that can be measured
	<p>Synthetic-aperture radar (SAR)</p> <p>Synthetic-aperture radar (SAR) is a form of radar that can be used to create two-dimensional or three-dimensional images of the Earth's surface. SAR provides a finer spatial resolution than conventional radar instruments. Outputs for the ocean include surface waves, sea ice monitoring and wind.</p>		<ul style="list-style-type: none"> Wind Surface waves Sea ice monitoring

Figure 3. Synthetic-aperture radar (SAR) for high-resolution monitoring of sea surface waves, wind, and sea ice.
Source: Copernicus Marine Service [2]

For operational management and oceanic research, satellite sensors are today a vital tool (Garcia & Wu, 2020). They address fundamental criteria including:

- Climate research and marine weather forecasts benefit from sea surface temperature (SST), collected from thermal infrared and microwave equipment (Smith, 2018).
- Precise sea level data and basic insights for the study of ocean circulation, abnormal warming events, or local subsidence as well as secular trend in average sea level increase from satellite altimetry (Davis et al., 2020).
- Ocean color lets one estimate phytoplankton concentration and, hence, indirectly primary production, so influencing the carbon cycle and the state of marine ecosystems (Garcia & Wu, 2020).

In this context of technological evolution, the SWOT (Surface Water and Ocean Topography) project was born, a joint satellite mission developed by NASA and CNES. Launched on 16 December 2022, SWOT is measuring the topography of the ocean with high accuracy, using

interferometry to produce a two-dimensional map (NASA/CNES, 2022). Observations from SWOT can be used to better understand ocean currents and processes at spatial scales on the order of 15–150 km, something that has not been done before (Brown et al., 2021).

On the other hand, acoustic instruments and coastal radar operate based on distinct physical principles that enable the remote monitoring of oceanic parameters (Wilson, 2018):

Acoustic Doppler Current Profilers (ADCPs) are placed either straight on the seabed, moored buoys, or on floating platforms. They estimate current velocity profiles along the water column at different depths using acoustic pulses emitted and Doppler shift analysis of the returning echoes. Providing high-resolution data vital for both coastal and deep-sea uses, ADCPs are extensively utilized for investigating ocean circulation, tidal fluxes, and turbulence dynamics (Miller et al., 2019).

By timing the flight of an acoustic pulse to the bottom and returning to the sensor, echosounders—**single-beam and multibeam sonars**—use sound waves to estimate seafloor depth and shape. While multibeam sonar systems generate many acoustic beams concurrently, covering a large swath of the seafloor, single-beam echosounders offer depth data straight underneath the vessel. Bathymetric mapping, habitat classification, underwater navigation—including submarine and autonomous underwater vehicle (AUV) operation—all depend on these technologies (Thompson, 2015).

Operating in either High Frequency (HF) or Very High Frequency (VHF) bands, **coastal radars** employ radio waves to track surface currents across significant coastal regions. By analyzing the Doppler shift in radio signals reflected by ocean waves, these devices can measure current velocities over an area extending tens of kilometers from the coast. For real-time observing of nearshore circulation, pollution dispersion, and search-and-rescue operations, they are especially useful (Wilson, 2018).

Remote observation has benefits in terms of broad, worldwide, or regional coverage as well as continuous monitoring guaranteed by satellite passing or radar station stability (Garcia & Wu, 2020). Large-scale, repeated frequency measurements enhance climatic and oceanic modeling by offering a data base spanning both time and space (Brown et al., 2021). The key constraints are the need for calibration and validation using in situ data and vertical resolution, usually inadequate for investigating deeper processes (Kim & Brown, 2021).

Recent years oceanography has been transformed by the synergy of in situ data and remote sensing data. While satellite observations give a global and continuous image of the ocean's condition, providing data with great spatial coverage, direct measurements are absolutely necessary for detailed knowledge of physical, chemical, and biological processes (Anderson et al., 2015). Through their combined integration, these approaches enable the development of numerically driven oceanographic models (Brown et al., 2021).

1.2 Research Aims and Objectives

1.2.1 Cross-validating SWOT altimetry with in situ measurements

The main objective of this work is to calibrate and validate (cal/val) the latest released version of SWOT altimetry data (Vignudelli et al., 2019). Although the technology has been revolutionary since its inception, remotely sensed data often contain systematic errors or biases in the correction algorithms (Davis et al., 2020). In this context, in situ data represent a crucial reference point for cal/val work (Anderson et al., 2015). Any calibration and validation effort thus depends on a consistent reference dataset, which in this case belong to an instrument called MVP (Moving Vessel Profiler), which makes it possible to obtain high-resolution vertical profiles of temperature, salinity and turbidity along the route of the ship (Vignudelli et al., 2019).

Although in situ data are widely recognized as essential for satellite cal/val, the literature still shows a lack on high-resolution comparisons between altimetric observations and in situ measurements at submesoscale and coastal levels. The MVP presents an unparalleled chance to obtain vertical profiles and this synergy of data sources has considerable potential to advance, yet such cross-validations have rarely been conducted over multiple transects in dynamic regions like the NW Mediterranean.

To address these questions, the work proceeds through a series of methodological steps. First, we compute dynamic height (DHC) from MVP profiles of temperature and salinity. This parameter can then be directly compared to the absolute dynamic topography (ADT) derived from SWOT sea surface height observations. Second, the two datasets' spatial and temporal scales are aligned using procedures including smoothing, filtering, and interpolation. Once co-located, geostrophic velocities are estimated using both the SWOT altimetric fields and the in situ profiles, therefore exploring how kinetic energy decays at various spatial scales. The calibration depends much on the comparison of these velocity fields since it indicates the magnitude and complexity of any detected discrepancies (Vignudelli et al., 2019). Then, statistical analysis (correlation coefficients, regression slopes, RMSE) measures the consistency between the two instruments (Foster et al., 2017). Finally, spectral and coherence analysis clarify scale-dependent variability—especially pertinent for the study of submesoscale characteristics (Brown et al., 2021).

The ultimate goal is not merely to highlight mismatches but to interpret and contextualize them. This work intends to suggest focused improvements for next cal/val campaigns by comprehending systematic errors (e.g., orbital or tidal corrections in SWOT data) and debating how methodological choices (e.g., choice of reference pressure, interpolation schemes) might introduce uncertainties (Kim & Brown, 2021). Such improvements could enhance the reliability of SWOT data for investigating submesoscale dynamics and coastal dynamics (NASA/CNES, 2022). In this sense, the work advances satellite-in situ integration in operational and research settings, as well as a better knowledge of the fundamental uncertainties in altimetry-based ocean data.

1.2.2 Research questions

The specific research questions directing this work include:

RQ1: How accurately do SWOT-derived sea surface height (SSH) and geostrophic velocities match those obtained from high-resolution MVP profiles in the NW Mediterranean?

RQ2: What are the main sources of discrepancy—are they primarily due to instrument limitations, processing methodologies, or genuine physical differences?

RQ3: Which smoothing, filtering, and interpolation approaches yield the most robust alignment of SWOT and MVP data in both time and space?

RQ4: How do mismatches in spectral analysis at different spatial scales inform our understanding of SWOT's performance in capturing submesoscale dynamics?

RQ5: Can systematic errors or biases in SWOT altimetry be mitigated through refined calibration procedures informed by in situ measurements?

2. Theoretical Background

2.1 Satellite Altimetry Basics

2.1.1 Altimetric Principles and Definitions (SSH, SLA, ADT)

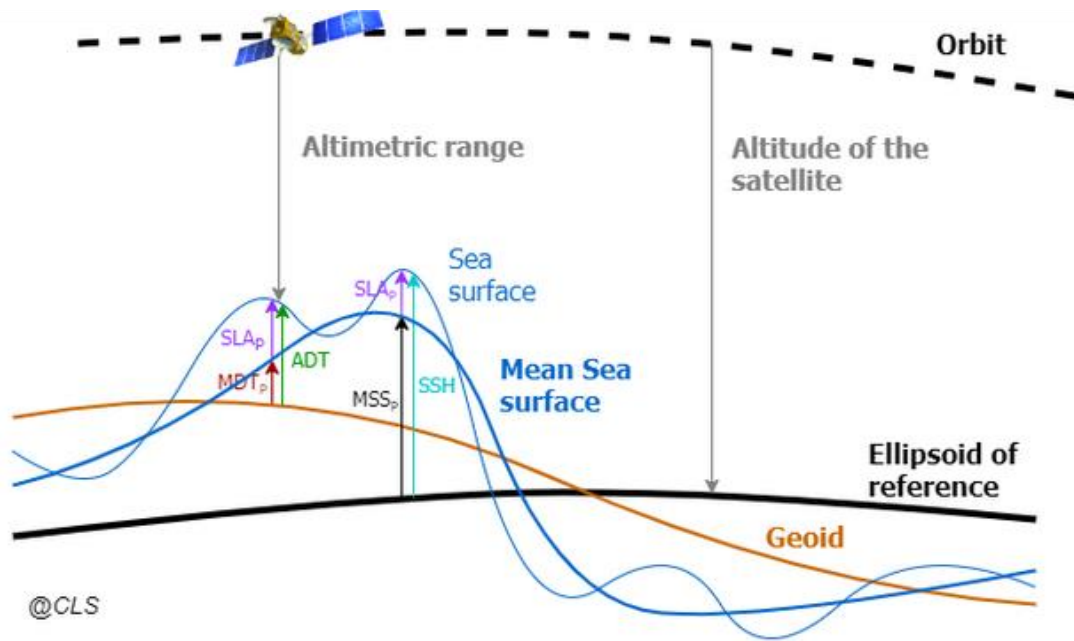


Figure 4. Reference surfaces and altimetric parameters used in satellite altimetry.
Source: Bessière [3]

Satellite altimetry is a technique for observing the ocean surface that relies on measuring the time it takes for a radar signal to travel from the satellite to the sea surface and back. The conversion of this time into a distance defines the range, the vertical distance separating the satellite from the ocean surface at a given moment. By use of this measurement, we can extract basic values for investigating ocean circulation, including absolute dynamic topography (ADT) and sea surface height (SSH). Reconstructing near-surface geostrophic velocity fields—a fundamental component of many oceanographic research—requires these values.

To determine the sea height relative to a global reference system, the altimeter measures two key parameters.

1. Measuring the round-trip time of a radar pulse with adjustments for atmospheric factors yields first the **range** (R), the distance between the satellite and the sea surface.
2. Second, with accurate orbit models (Fu and Cazenave, 2001; Chelton et al., 2011) and orbital positioning methods including GPS, DORIS, and laser tracking, the **altitude of the satellite** (H) relative to the reference ellipsoid, is ascertained with great precision (on the order of millimeters).

These observations define the sea surface height relative to the ellipsoid as:

$$\text{SSH} = R - H \quad (1)$$

Every further altimetric computation is based on this relationship.

Considered as the instantaneous height of the sea level relative to the reference ellipsoid—typically WGS84 in many datasets—sea surface height (SSH) is, at first approximation, the sum of two contributions:

1. The first is the geoid height, which is the elevation of the geoid above the ellipsoid. The geoid is the equipotential surface of the Earth's gravitational field that best approximates the mean sea level at rest. Though the geoid shows notable spatial fluctuations—on the order of hundreds of meters globally—its temporal variations are rather slow and usually inconsequential over durations of months to years (Sandwell and Smith, 2009).
2. The second contribution is dynamic topography (DT), which is the deviation of the sea surface from the geoid due to external forces such as wind, temperature, salinity, and steric effects, as well as ocean circulation. Including geostrophic currents, eddies, and fronts, DT carries the oceanographic data of relevance (Le Traon and Morrow, 2001).

SSH can thus be written as:

$$\text{SSH} = \text{Geoid} + \text{DT} \quad (2)$$

Two further parameters describe the separation between the mean and variable components. Calculated over lengthy intervals, such years, the mean sea surface (MSS) is the average SSH and reflects the worldwide mean shape of the ocean surface. By subtracting the geoid from the MSS, one obtains the mean dynamic topography (MDT). Crucially for climate-scale studies, MDT stands for the stationary circulation brought about by radiative balance, constant winds, and Earth's rotation as well as other permanent influences (Rio et al., 2014).

Sea level anomaly (SLA) is defined as the difference between the instantaneous SSH and the reference MSS over a specified period (P). In plain terms, $\text{SLA} = \text{SSH} - \text{MSS}(\text{P})$. This quantity highlights transitory events like tides, planetary waves, seasonal currents, and steric fluctuations, so capturing the temporal variability of sea level. SLA separates the variability owing to dynamic oceanic processes (Cipollini et al., 2017), since MSS already includes the mean (and indirectly the geoid contribution).

Absolute dynamic topography (ADT) is the dynamic component of the sea surface relative to the geoid at a given time. Practically, ADT is computed as $\text{ADT} = \text{SSH} - \text{Geoid}$ in case a sufficiently exact geoid model is given. However, because fine-scale knowledge of the geoid is often limited, the mean dynamic topography (MDT) is frequently used as a reference, leading to the formulation $\text{ADT} = \text{MDT} + \text{transient fluctuations}$. Many operational altimetric datasets include ADT in the form $\text{ADT} = \text{MSS} - \text{Geoid} + \text{SLA}$; this can be changed to $\text{ADT} = \text{MDT} + \text{SLA}$ (with $\text{SLA} = \text{SSH} - \text{MSS}$). This method stresses the rapid variability by using the "mean" geoid buried in MDT (Le Traon et al., 2015).

Since they directly indicate the surface pressure gradient and, hence, geostrophic velocity, SLA and ADT are the major altimetric products in operational and research oceanography. In the framework

of this work, ADT produced from altimetric missions—including SWOT as well as conventional missions such as Jason or Sentinel-3—is evaluated against in situ dynamic topography estimates obtained from temperature and salinity profiles acquired by the MVP.

The definitions of SSH, SLA, and ADT within this paper have two uses. They allow the investigation of fine-scale oceanic features as well as the reconstruction and comparison of in situ dynamic topography estimates—generated from temperature and salinity profiles—with ADT products acquired from SWOT and other missions (DUACS). SWOT's enhanced spatial resolution allows one to investigate submesoscale fronts and vortices, often missed by classical altimetric missions because of their sparser spatial sampling. Thus, a correctly computed and validated ADT becomes a necessary instrument for exploring oceanic dynamics on distances of only few kilometers.

Knowing these definitions helps one to build the theoretical framework for the studies discussed in later chapters. Chapter 2.2 will show, for example, how horizontal gradients in ADT can be used to predict near-surface geostrophic velocities; Chapter 5 will provide the findings of comparisons between altimetric fields and MVP in situ observations. Evaluating the quality of SWOT results depends on this integration, particularly in settings like the Northwestern Mediterranean Sea marked by submesoscale variability.

2.1.2 Challenges: Accuracy, Coastal Contamination, Instrumental Noise

Reaching the necessary degree of accuracy to record fine-scale ocean features is one of the main difficulties in satellite altimetry. Particularly in areas where the water circulation shows fast spatial and temporal variability, even subtle errors—on the order of a few centimeters—may mask the dynamic signals of relevance. Achieving this precision requires accurate orbital determination, strong altimeter electronic component calibration, and reliable correction models for atmospheric path delays (Fu and Cazenave, 2001). These errors may become rather significant at the submesoscale, so restricting our capacity to completely resolve smaller, rapidly evolving oceanic structures.

Still, a major cause of ambiguity is orbit determination; while methods as DORIS, GPS, and satellite laser ranging have significantly raised orbital accuracy, any residual mistake in the calculated satellite height immediately results in an error in sea surface height. This is especially critical near complex geoid gradients, where local variations in Earth's gravitational field can amplify small orbit-related biases. Furthermore, the geoid itself—as discussed in Section 2.1.1—is not exactly known at high resolution; this restriction complicates the separation of the mean gravitational signal from the dynamic contributions of interest.

As the altimeter's footprint crosses or approaches the sea-land barrier, coastal altimetry adds other challenges. Land returns can pollute the radar echo, therefore producing false range estimations between the satellite and, for example, a lake surface (Cipollini et al., 2017). Advanced waveform retracers and specialized coastal processing methods have been developed to address this issue (Vignudelli et al., 2019), but challenges persist where tidal flats, steep topography, or complex coastlines render classical algorithms unreliable.

Retrievals of sea surface height are likewise influenced by instrumental and ambient noise. This can be caused by thermal changes in the radar hardware, variations in transmit power, and sea state biases (associated to wave height and wind speed). Usually, calibration, waveform retracking, and statistical filtering (le Traon et al., 2015) help to offset these effects. Still, residual noise can hide

weak signals in the altimeter data, especially when looking at finer scales of motion or trying to find subtle height changes linked with submesoscale features.

The upcoming generation of wide-swath altimeters, most notably SWOT, represents a major step forward in addressing several of these issues (Morrow et al., 2019). SWOT lowers aliasing issues and permits more robust identification of small-scale oceanic events including coastal currents and submesoscale eddies by offering two-dimensional observations at higher spatial resolutions. However, careful attention to error sources—especially orbit precision, geoid modeling, and the specialized correction algorithms required in coastal zones—remains crucial if one is to fully maximize this leap in observation capability.

2.2 Geostrophic Velocity Theory

2.2.1 Fundamental Equations

Geostrophic motion forms the cornerstone of large-scale and mesoscale ocean dynamics, providing a fundamental framework for interpreting circulation patterns in terms of the interplay between pressure gradients and the Coriolis force. In its simplest form, geostrophy suggests that horizontal acceleration is minimal compared to the balance between the horizontal pressure gradient and the Coriolis force. On time scales where inertial oscillations average out and on scales greater than a few tens of kilometers (mesoscale), this approximation is valid. It provides a strong basis for tying near-surface currents (Gill, 1982) with fluctuations in sea surface height (SSH) seen by satellite altimetry.

Earth's rotation generates the Coriolis force, which causes flowing fluid to appear to deflect to the right in the Northern Hemisphere and to the left in the Southern Hemisphere. Mathematically, the Coriolis acceleration is derived from the horizontal velocity vector v and the Coriolis parameter f :

$$a_C = f k \times v \quad (3)$$

- where k is the upward-pointing unit vector (Pedlosky, 1987).
- The Coriolis parameter f is defined as $f = 2\Omega \sin\phi$, with Ω being the angular velocity of the Earth's rotation and ϕ the latitude. Over mid-latitude or basin-scale extents, variations in f with latitude may introduce the so-called β effect, critical for understanding planetary waves and large-scale current meanders.

The horizontal pressure gradient in the ocean is primarily driven by surface height gradients and density variations, which result from temperature and salinity gradients. The vertical stratification is strong enough over most of the open ocean to establish hydrostatic equilibrium, in which case vertical accelerations are minor relative to the force of gravity (Stewart, 2008). As a result, the slope of the sea surface itself can help approximate the horizontal pressure gradient close to the surface. A steeper ocean surface slope leads to a larger horizontal pressure gradient and consequently a stronger geostrophic flow, establishing a conceptual link between geostrophic currents and satellite-altimeter-measured SSH fields.

Under steady-state geostrophic balance, the horizontal momentum equations in vector form shrink to:

$$-fv = -\frac{1}{\rho} \frac{\partial p}{\partial x}, \quad fu = -\frac{1}{\rho} \frac{\partial p}{\partial y} \quad (4)$$

Where ρ is the seawater density (commonly approximated as a constant in geostrophic treatments)

- u and v are the velocity components in the eastward and northward directions, respectively
- p is the pressure (Gill, 1982)

Velocity is aligned perpendicular to the direction in which pressure varies most rapidly, thus stressing the orthogonal nature of the Coriolis force and the pressure gradient in a simple geostrophic flow.

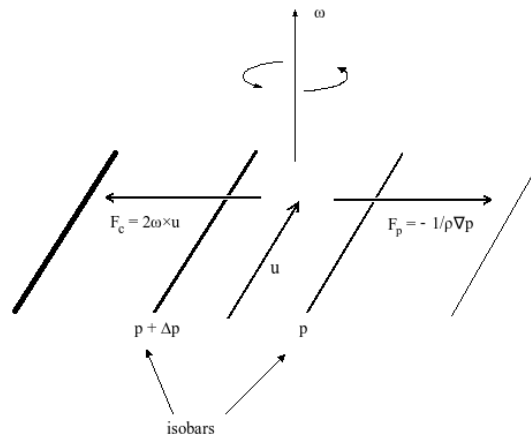


Figure 5. Diagram of the geostrophic balance in the Northern Hemisphere, showing the pressure gradient force, Coriolis force, and resulting geostrophic flow parallel to isobars.

Source: Wikipedia [4]

Expanding the pressure at a particular depth z in the ocean helps to understand these momentum equations in terms of surface height as:

$$p(z) \approx p_0 + \rho g \eta + p_0(z) \quad (5)$$

- g is gravitational acceleration
- η is the sea surface elevation relative to a reference level (Cushman-Roisin and Beckers, 2011)
- p_0 is the atmospheric pressure at sea level
- $p_0(z)$ represents the baroclinic terms

The gradient of the pressure in the horizontal directions close to the surface is then tightly related to $\Delta\eta$. This implies that, under geostrophy, the velocity field can be deduced from the slope of η , which is directly connected to SSH in altimetric data.

Geostrophy still prevails in the ocean interior whenever the Rossby number—the ratio of inertial to Coriolis forces—remains minimal (Pedlosky, 1987). Usually, this assumption is true for slow, large-scale flows. However, near strong current systems or submesoscale fronts, the Rossby number can rise to values where geostrophic balance loses accuracy. Notwithstanding these localized

deviations, most satellite altimetry-derived velocity data are generated from the geostrophic approximation, which remains the basic theoretical underpinning for understanding wide oceanic circulation.

Geostrophic flows are fundamentally rotational around high- and low-pressure (or, equivalently, high- and low-elevation) centers rather than moving directly from high to low surface elevations. In the Northern Hemisphere, for example, counterclockwise (cyclonic) circulation is linked with low sea-level anomalies, while clockwise (anticyclonic) geostrophic currents are usually linked with high sea-level anomalies. Much of the eddy and front detection done with altimetric observations depends on this relationship (Chelton et al., 2011).

Potential vorticity conservation is another concept pertinent to geostrophy, as it extends the geostrophic balance to include stratification and variations of f with latitude. Although the exact derivation of potential vorticity is beyond the scope of this discussion, the key point is that variations in column thickness or latitude can alter circulation patterns while approximately preserving geostrophic balance. In areas like the Northwestern Mediterranean, where the interaction of bathymetry, shoreline shape, and water mass characteristics can alter local circulation, this idea becomes even more relevant (Millot and Taupier-Letage, 2005).

Within the framework of this thesis, the geostrophic approximation offers the theoretical means for converting SSH fields into velocity estimations. One can extract near-surface current patterns by applying these basic equations to altimetric products (e.g., SWOT data or traditional nadir altimetry), which can then be compared against in situ readings from the MVP. This synergy between satellite-based fields and in-water observations supports the broader objectives described in later chapters concerning fine-scale circulation analysis and data validation, and it helps define mesoscale and submesoscale processes.

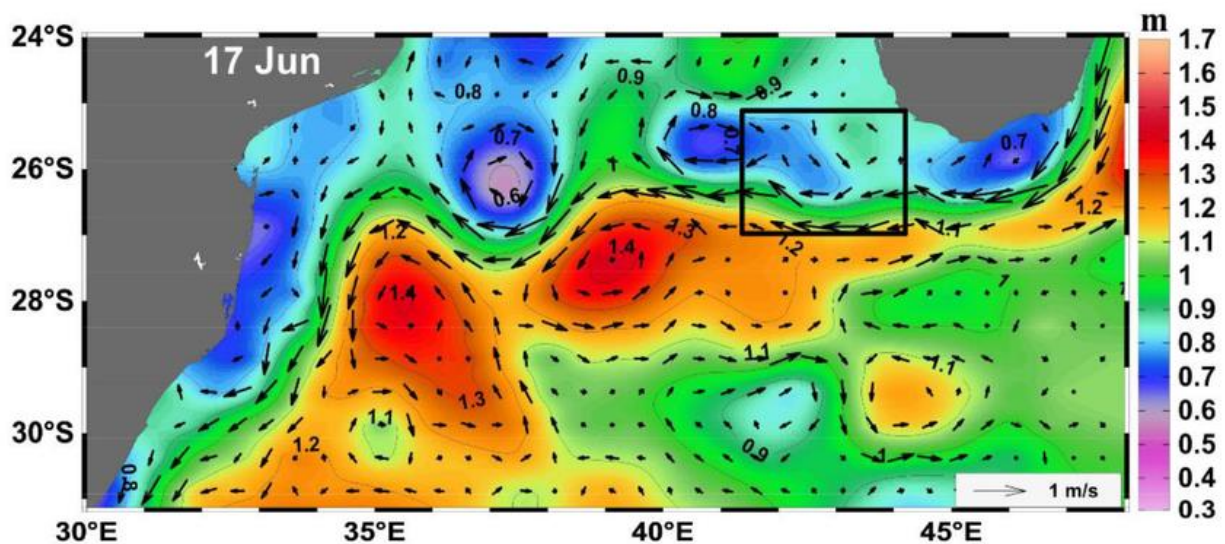


Figure 6. Sea surface height (SSH) visualized with color-graded contours and derived geostrophic velocity vectors (black arrows) from satellite altimetry in the Pacific Ocean.
Source: Lamont, Barlow, & Brewin, 2018 [5]

2.2.2 Practical Computation (From SSH Gradients to Surface Velocity)

From altimetric measurements, geostrophic velocity is computed practically by translating sea surface height gradients into a horizontal flow field. Raw SSH measurements (or related products such as absolute dynamic topography, ADT) are first gridded or interpolated to produce a continuous surface in standard processing stages. To approximate the horizontal pressure gradient from these grids, partial derivatives of SSH in the zonal (x) and meridional (y) directions are computed.

Under geostrophic balance, the velocity can be expressed as the SSH gradient's equivalent:

$$u_g = -\frac{g}{f} \frac{\partial \eta}{\partial y}, \quad v_g = \frac{g}{f} \frac{\partial \eta}{\partial x} \quad (6)$$

- η is the sea surface height
- u_g and v_g are geostrophic velocity components in the eastward and northward directions
- g and f have their typical physical meanings

These equations illustrate that velocity is perpendicular to the SSH gradient, with its magnitude proportional to the slope of the sea surface.

Altimetric products must undergo several corrections before these derivatives are computed. If not properly managed, atmospheric path delays (both dry and wet tropospheric, ionospheric), tidal corrections, and instrumental biases can each introduce inaccuracies that affect velocity estimations (Pujol et al., 2016). Reconstructing the two-dimensional SSH field from wide-swath observations and verifying that swath discrepancies or tilts are minimized helps reduce errors in SWOT data (Morrow et al., 2019). Consequently, a more consistent picture of geostrophic velocity over the research area is achieved once these corrections are applied.

Finally, geostrophic velocity fields produced by SSH can be verified and calibrated using in situ measurements—including dynamic heights derived from temperature and salinity profiles, current profilers, or drifting buoys. This study uses the Moving Vessel Profiler (MVP) to produce steric height by integrating temperature-salinity (and hence density) data. By comparing the MVP-based steric height gradients with satellite-based SSH gradients, we gain insight into the consistency and precision of altimetric geostrophic velocities.

Refining the geostrophic velocity fields and evaluating any systematic offsets or scale-dependent inaccuracies rely on these validation methods. In subsequent chapters, we will investigate how differences between MVP-based measurements and altimetric data could reveal either residual problems in altimetric products or local deviations from geostrophy. This computation chain—from raw altimetric readings to velocity fields—thus underpins much of the research presented in this work.

2.2.3 Approximations and Reliability at Smaller Scales

As one advances to smaller spatial scales (submesoscale, on the order of 1–10 km) or faster-evolving phenomena, the geostrophic approximation loses accuracy, even though it is robust for large-scale flows and mesoscale events. The Rossby number can approach or exceed unity at these scales, suggesting that ageostrophic dynamics, inertial forces, and frictional forces also become important (Thomas et al., 2008). Among these consequences are frontogenesis, mixed-layer

instabilities, and Ekman-driven flows—each potentially causing non-negligible deviations from purely geostrophic motion.

Topographic restrictions, freshwater inputs, nearshore dynamics, and coastal areas can further challenge the geostrophic assumption. Strong horizontal shear and vertical velocity components generated by abrupt bathymetric shifts or shoreline anomalies are not captured by conventional geostrophic models. Similarly, strong density gradients resulting from river outflow or localized upwelling can skew the local pressure field in ways that altimetry—with its limited temporal resolution—cannot readily discern (Cazenave and Schaeffer, 2018).

The temporal sampling of satellite altimetry adds another constraint. Conventional altimeters, including Jason-type missions, can alias quicker submesoscale processes since their repetition cycles are on the order of 10 days or more. With its broad-swath coverage, SWOT offers superior resolution; however, if some features evolve on daily or sub-daily scales, even SWOT may suffer from undersampling. Therefore, the reliability of geostrophic velocity estimates at smaller scales depends on both the satellite sampling properties and the accuracy of high-resolution corrections, such as wet tropospheric or sea state bias adjustments (Dufau et al., 2016).

Notwithstanding these challenges, the geostrophic framework remains a useful starting point, as it provides a first-order understanding of marine flow. Combining in situ measurements—such as MVP-based dynamic heights—allows researchers to pinpoint areas where the geostrophic balance requires adjustment or breaks down. These comparisons are conducted to assess the validity of altimetry-derived velocity fields in the Northwestern Mediterranean, where submesoscale processes might play a significant role in heat and nutrient transfer, eddy development, and energy cascades. Understanding the limits of geostrophy at smaller scales helps guide the interpretation of surface currents generated from SWOT as well as the design of future observational campaigns.

2.3 Fine-Scale Oceanographic Structures

2.3.1 Fronts, Eddies, and Submesoscale Perturbations: Definitions

Fine-scale oceanographic structures are features that appear at relatively small horizontal scales—of the order of a few kilometers (km) to few tens of km—and tend to evolve over relatively rapid timescales (tens of minutes). These include fronts, eddies and other submesoscale perturbations. While mesoscales (50 to 200 km order) structures are the dominant force in large scale circulation, smaller scales are increasingly acknowledged to influence biological productivity, heat transport and vertical mixing (Klein & Lapeyre, 2009). They also represent channels through which energy flows from large to small scales.

As defined in oceanography, a front is a narrow boundary zone between two water masses with contrasting properties (density, temperature, or salinity) (Rousselet et al., 2019). Upon meeting a front, the water masses typically maintain their identities, thus generating strong horizontal gradients that affect the local circulation. These steep gradients can amplify vertical motions in the upper ocean, promoting the exchange of nutrients between surface and subsurface layers, ultimately affecting phytoplankton and zooplankton distributions (Levy et al., 2012).

In many field campaigns, physical gradients alone do not necessarily delimit front boundaries in their entirety; biological markers can be just as informative (Oms et al., submitted). In the context of this thesis, the front of interest was not measured by the author, but by Laurina Oms, et al. using a statistical analysis of organism distributions. Oms and collaborators described changes in both phytoplankton and other planktonic communities across the upper layers of the sea as an integrated boundary that coincided with salinity gradients in the Northwestern Mediterranean Sea (Oms et al., submitted). Their results highlight how incorporating biophysical approaches can enhance the resolution at which fine-scale frontal zones can be observed.

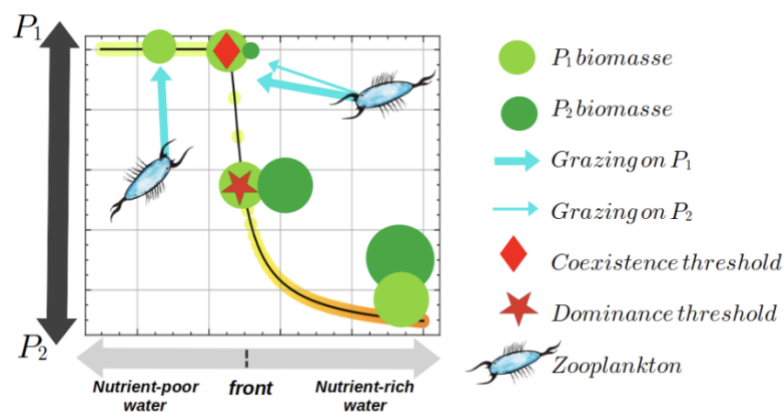


Figure 7. Conceptual diagram of planktonic community responses across a nutrient gradient at a frontal zone.
Source: Oms et al. [6]

Eddies are coherent rotating water masses that are generally classified as cyclonic or anticyclonic, depending on the sign of their vorticity (Chelton et al., 2011). The duration of mesoscale eddies can range from weeks to months, and they can be tens to hundreds of kilometers across. Instead, submesoscale eddies may have diameters of only a few km with much shorter lifetimes (Thomas et al., 2008). They frequently grow at the boundaries of the fronts and filaments where the horizontal density gradient is enhanced. Eddies are key players in lateral transport of heat and nutrients, as they lead to localised upwelling (in cyclonic eddies) or downwelling (in anticyclonic ones).

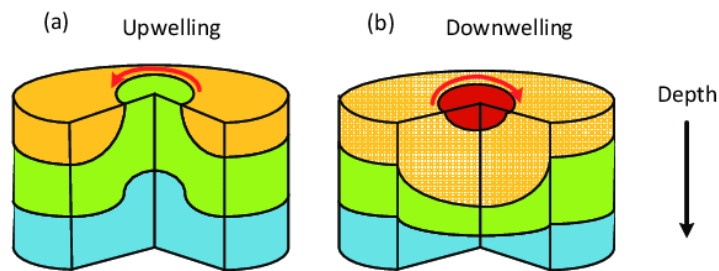


Figura 8 Schematic 3D diagram illustrating vertical motions associated with (a) cyclonic eddies, which induce upwelling, and (b) anticyclonic eddies, which cause downwelling.
Source: Liu et al., 2021 [7]

Besides such well-defined fronts and coherent eddies, submesoscale perturbations also include filaments, meanders, and transient vortices. These features can drive large bursts of vertical velocity—often order of meters per day—beyond what is normally observed in the deep ocean (Klein & Lapeyre, 2009). These phenomena facilitate exchanges of nutrients, trace gases, and plankton with the deeper layers, having significant effects on surface productivity and carbon export.

These smaller-scale processes are disproportionately relevant to marine ecosystems. Fronts can concentrate plankton, enhance predator-prey interactions, and increase local productivity. Eddies, in contrast, can entrain and disperse organisms and/or nutrient-rich waters, modifying growth conditions within their interior (Thomas et al., 2008). These complexities are compounded by submesoscale perturbations, which can intermittently upwell nutrients into the euphotic zone (Levy et al., 2012). Overall, these fine-scale features create ecological niches that may differ sharply from surrounding waters, as modelled by Oms et al. (2024) in the Mediterranean Sea.

2.3.2 Observational Evidence (Vertical Profiles, Surface Patterns)

Eddies are often identifiable by their typical vertical profiles. For example, in cyclonic eddies the depression of isopycnals toward the surface may localize upwelling and result in the upward transport of colder, nutrient-rich waters (Thomas et al., 2008). In comparison, in anticyclonic eddies isopycnals dome downward and are associated with downwelling of surface waters (Rousselet et al., 2019). In the context of this work, vertical profiles generated by the Moving Vessel Profiler (MVP) (and processed by Melvil Bessiere) are crucial observational evidence. Temperature and salinity anomalies of these profiles are compared to identify the different types of eddies present in the region of study.

Remote sensing products, especially Absolute Dynamic Topography (ADT) grids, help the surface circulation features to be visually identified. Cyclonic eddies generally exhibit negative anomalies in ADT (reduced height of sea surface), while anticyclonic eddies reveal positive anomalies (Chelton et al., 2011). A gridded ADT plotted over time can thus reveal the presence, intensity, and evolution of vortices. In this thesis we use SWOT-based ADT products to identify these eddies and submesoscales patterns, supporting or contrasting MVP-derived signatures.

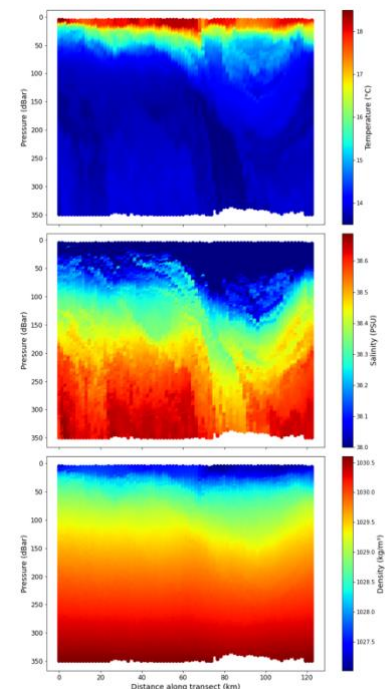


Figura 9. Vertical sections of temperature (top), salinity (middle), and density (bottom) obtained from MVP transect 13. The downward doming of isopycnals is consistent with the presence of an anticyclonic eddy and associated downwelling.
Source: Bessière, [8]

The coherence of ocean dynamics can be investigated in more detail by overlaying vertical profiles derived from MVP data on surface maps generated from ADT data. Cyclonic eddies are identified by upwardly tilting isopycnals and negative ADT centers while anticyclonic eddies show the inverse pattern. Frontal segments—defined initially by sharp gradients in ADT text—typically correspond to high gradient regions in MVP temperature or salinity data. This convergence of remote sensing patterns with in situ vertical profiles strengthens our interpretation of the regional circulation and provides accurate observational evidence of fine-scale process in the Northwestern Mediterranean (Rousselet et al., 2019; Oms et al., 2024).

2.4 Spectral Analysis and its Role in Oceanography

2.4.1 Spectral Analysis Fundamentals

A mathematical tool used to decompose a time or spatial series into its component frequencies, spectral analysis offers insight into the fundamental processes generating variability at various scales (Emery and Thomson, 2001). Spectral analysis is extensively used in oceanography to detect dominant scales of motion (e.g., tidal bands, mesoscale eddy scales, submesoscale fluctuations) from signals such as sea surface height, velocity components, or temperature records.

Spectral analysis is based on the theory that a physical signal can be expressed as a sum of sinusoids (waves) with various frequencies and amplitudes. We assume that if $x(t)$ is a time or space series of sea surface height (SSH) or another parameter of interest, then:

$$x(t) = \sum_{n=0}^{N-1} a_n \cos(\omega_n t) + b_n \sin(\omega_n t) \quad (7)$$

with a_n and b_n as the coefficients and ω_n the angular frequency of the n -th sinusoid. This process examines how much variability the signal contains at each frequency by converting $x(t)$ into the frequency domain.

Oceanographic data are typically sampled spatially or discretely in time. From a finite array $x(k)$, where k is the sample index, the Discrete Fourier Transform (DFT) produces an array of complex Fourier coefficients $X(f)$:

$$X(f) = \sum_{k=0}^{N-1} x(k) e^{-2\pi i \frac{fk}{N}} \quad (8)$$

with N as the total number of samples. Press et al. (2007) find that the Fast Fourier Transform (FFT) is an efficient method for computing the DFT in $O(N \log N)$ time, making it suitable for large oceanographic datasets.

Often, preprocessing is necessary to reduce numerical artifacts before applying the FFT. Typical procedures include:

- Eliminating low-frequency or linear trends that might dominate the spectrum, thereby removing spurious spectral energy.
- Multiplying the original data by a window function—such as Hann—to reduce "leakage" in the spectral domain. Sharp discontinuities at the data edges can cause false frequencies;

windowing tapers the endpoints of the time series, thereby enhancing the resolution of actual spectral peaks (Emery and Thomson, 2001).

The Power Spectral Density (PSD), $P(f)$, quantifies how signal power (or variance) is distributed among frequencies once the Fourier coefficients $X(f)$ are obtained:

$$P(f) = \frac{|X(f)|^2}{N\Delta t} \quad (9)$$

where Δt is either the spatial sampling distance for spatial data or the sampling interval for time series. Usually shown on a log-log scale, the PSD reveals power-law behaviors or distinct peaks associated with specific oceanic phenomena (e.g., tides, inertial oscillations, mesoscale variability).

Spectral analysis helps separate signals at various scales in SSH data—from in situ instruments or satellite altimetry. For instance, we might observe peaks at diurnal or semidiurnal frequencies (tidal components), mesoscale peaks at periods of tens of days, or submesoscale signatures at higher frequencies (Le Traon and Morrow, 2001). Typically, the evaluation of altimetric SSH data involves choosing a transect or time series, preprocessing for artifacts (e.g., tides, atmospheric adjustments), and subsequently using the FFT to derive the PSD.

Welch's methodology (Welch, 1967) is used to improve spectral estimation, particularly when dealing with noisy oceanographic signals. The data are divided into overlapping segments, each windowed, and the spectra of these segments are averaged, generating a smoother PSD curve. In oceanography, ensemble averaging—integrating several segments from different areas or data records—is also employed, thus enhancing the statistical reliability of the spectral estimate.

Two-dimensional (2D) spectrum analysis is crucial when analyzing spatial fields (e.g., 2D SWOT measurements of SSH), even though much of spectral analysis is explained in a one-dimensional context (time or space). A 2D Fourier transform decomposes the signal into wavenumbers k_x and k_y . The resulting 2D power spectrum shows how variance is distributed across various geographical scales in both the east-west and north-south directions, thereby clarifying anisotropy in oceanic structures such as fronts or jets (Callies and Ferrari, 2013).

Sometimes, the phase spectrum and cross-spectral analysis provide further information, such as the phase relationship between two signals (e.g., SSH and another oceanographic variable). The coherence measures the extent to which one signal explains the fluctuations in another at a given frequency (Bendat and Piersol, 2011).

2.4.2 Why Spectral Analyses Are Relevant for Identifying Oceanic Features

Surface geostrophic velocity is proportional to the gradient of SSH, so the spectral characteristics of velocity fields are intrinsically linked to those of SSH (Le Traon et al., 2015). Examining velocity spectra allows oceanographers to identify distinct bands corresponding to mesoscale eddies, submesoscale instabilities, or near-inertial oscillations. Deviations from predicted spectral slopes (e.g., $-5/3$ or -3 power laws in *figure 11*) can indicate strong frontal dynamics or ageostrophic circulation.

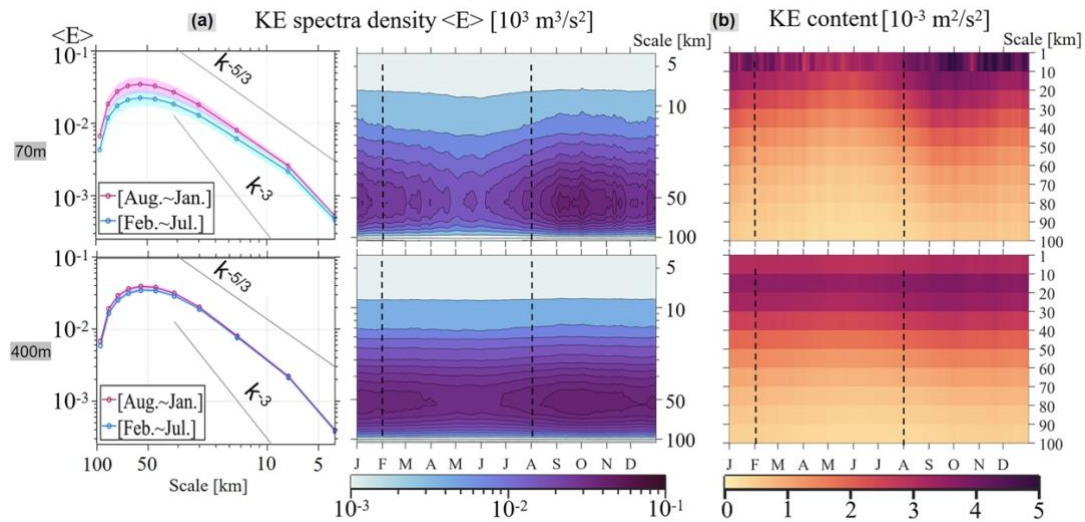


Figura 10. Spectral analyses of kinetic energy (KE), showing spectral density (a) and total energy content (b) as a function of scale and time. The panels illustrate seasonal variations and vertical differences between surface and deeper layers.

Source: AGU Publications [9]

Typically, mesoscale eddies dominate the maritime energy spectrum at wavelengths of hundreds of kilometers, while turbulence and ageostrophic processes contribute significantly to the velocity field at submesoscale ranges ($\sim 1\text{--}10$ km). For understanding energy dissipation and nutrient flow in near-surface waters, spectral analysis is thus a potent diagnostic tool for assessing how energy cascades from large to smaller scales.

Measurement noise in the velocity field obtained from altimetry or in situ devices can obscure true ocean signals at certain scales (Morrow et al., 2019). By identifying flat or unphysical spectral levels at high frequencies, spectral analysis separates genuine oceanic variability from random noise. Given emerging missions like SWOT, which aim to resolve finer scales than conventional altimeters, this capability is especially important.

Cross-spectral coherence can highlight processes such as frontal upwelling or eddy-induced biological responses (Klein and Lapeyre, 2009) and reveal connections between velocity and other parameters—such as temperature, salinity, or chlorophyll content. High coherence at submesoscale frequencies may indicate strong, localized interactions between physical and biogeochemical processes, which is crucial for understanding local marine ecosystems.

Spectral analyses thus provide a valuable diagnostic tool in Chapters 4 and 5 of this paper, where we explore the energy distribution across scales for both satellite-derived and MVP-derived observations. In particular, at submesoscale wavelengths we seek to assess how closely SWOT-based altimetry matches in situ measurements by comparing PSDs. This comparison helps identify regions where further calibration or methodological improvements are needed, as well as the capability of SWOT to capture fine-scale changes in the Northwestern Mediterranean.

3. Missions and Campaigns

3.1 SWOT Mission

3.1.1 Historical Perspective of Satellite Altimetry and the “Revolution” of SWOT

Originally developed in the 1970s, satellite altimetry began with the first dedicated missions such as GEOS-3 and SEASAT, which offered early glimpses into the viability of measuring sea surface height from space. Despite technical challenges such as instrument noise, orbital errors, and atmospheric signal distortions, these pioneering satellites established that radar pulses could precisely estimate the distance between the satellite and the ocean surface (Fu and Cazenave, 2001). Improved orbit determination and altimeter design over time produced missions like TOPEX/Poseidon, which represented a quantum leap in altimetric precision and global coverage.

Subsequent missions—ERS-1/2, the Jason series, Envisat, CryoSat-2, and Sentinel-3—further refined altimetric measurement methods, thereby increasing the resolution and precision of sea surface height datasets. Collectively, these projects have enabled researchers to monitor sea level rise, ocean currents, and major climate events with unprecedented accuracy (Chelton et al., 2011). Traditional altimeters, however, measure only a limited swath directly beneath the satellite (nadir), which restricts their geographical coverage and makes it challenging to resolve fine-scale features in coastal zones or submesoscale dynamics.

As scientists sought to fill in the spatial gaps inherent in nadir systems, the concept of wide-swath altimetry gained popularity. Measuring the sea surface over a wider swath would allow for more continuous capture of two-dimensional surface height variations, thereby reducing aliasing errors and enabling a more complete characterization of mesoscale and submesoscale processes (Morrow et al., 2019). This concept paved the way for the Surface Water and Ocean Topography (SWOT) project.

Under the leadership of NASA (United States) and CNES (France), with contributions from CSA (Canada) and UKSA (United Kingdom), SWOT is the result of an international collaboration. Building on the experience gained from TOPEX/Poseidon and Jason missions, the SWOT project introduced novel engineering approaches to achieve two-dimensional radar interferometry in space (Esteban-Fernández, 2013). Its design and scientific goals reflect decades of development in altimetric technology, data processing, and the recognition that fine-scale ocean dynamics significantly affect global circulation and climate.

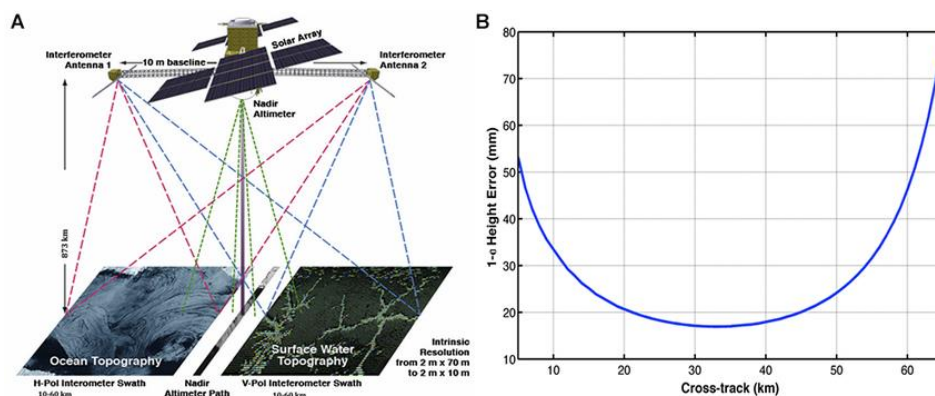


Figure 11. Strengths and constraints of SWOT in observing coastal and submesoscale ocean dynamics. (A) Principle of wide-swath interferometric altimetry, (B) corresponding variation in measurement error across the swath.

Source: Esteban Fernández [10]

Dubbed a "revolution" in satellite altimetry, SWOT seeks to close a long-standing observational gap by providing unprecedented detail in estimating sea surface height over large areas. Beyond oceanography, SWOT also targets measurements of freshwater bodies—including rivers and lakes—thus bridging the gap between traditional open-ocean altimetry and inland hydrology. This broader scope highlights the transformative potential of uniting several research communities under a single, high-resolution observational platform (Biancamaria et al., 2016).

3.1.2 Measurement Principles, Coverage, and Data Products

A new tool designed to simultaneously monitor two swaths on either side of the spacecraft nadir, the Ka-band Radar Interferometer (KaRIn) forms the core of SWOT. Operating at Ka-band (~35 GHz), the device transmits radar pulses toward the sea surface, which are received by two separate antennas. By measuring the phase difference between the signals at each antenna, KaRIn deduces the height of the water surface over a broad swath—on the order of 50 km to either side of nadir—thereby enabling a total coverage width of approximately 100 km (Esteban-Fernández, 2013).

Timing the radar pulse reflection at a single antenna determines the range to the ocean in conventional nadir altimetry. In contrast, SWOT's interferometric technique measures the path difference between two antennas separated by a defined baseline. From the geometry of the returned signal, one can determine the height h if ϕ is the interferometric phase and B the baseline. With a nominal accuracy target of a few millimeters (Morrow et al., 2019), the interferogram generated by combining the signals from both antennas provides precise information about the surface elevation profile.

The orbit of SWOT is designed to maximize both temporal revisiting and spatial coverage. At an altitude of roughly 890 kilometers, the satellite follows an orbit with an inclination that enables near-global coverage between approximately 78°S and 78°N. By acquiring repeated wide-swath images of the ocean surface, a repetition cycle of about 21 days captures changes resulting from mesoscale and submesoscale dynamics. This high spatio-temporal resolution contrasts sharply with the single-track coverage of traditional altimeters, potentially resolving features on scales of a few kilometers.

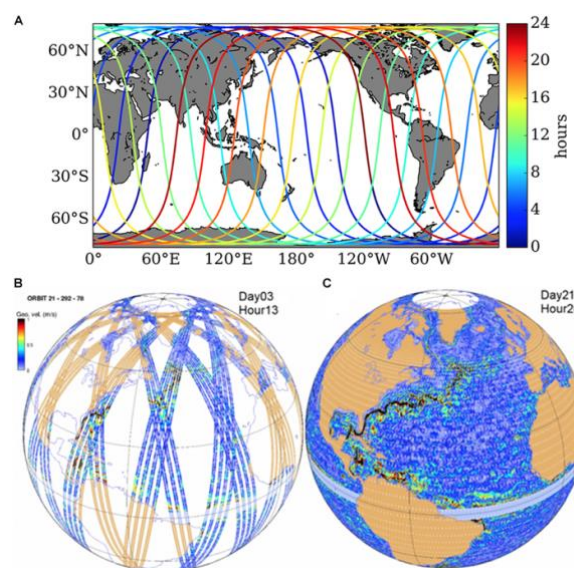


Figure 12. SWOT's orbital design enables near-global coverage between 78°S and 78°N with high spatial and temporal resolution. (A) One-day orbital swaths and revisit times; (B–C) coverage patterns over a full 21-day cycle.

Source: Morrow et al., 2019 [11]

SWOT data packages span from Level-1 interferometric observations (raw signal phase and amplitude) to Level-2 and Level-3 geophysical variables. By correcting for atmospheric delays, sensor biases, and geophysical effects, the gridded sea surface height (SSH) map is produced—providing the primary output of immediate importance to oceanographers (Esteban-Fernández, 2013). For ocean circulation analysis, users can extract absolute dynamic topography (ADT), sea level anomalies (SLA), and geostrophic velocity estimates from these SSH fields. SWOT will also deliver water surface elevation data for rivers and lakes to support hydrological applications, thereby enabling cross-disciplinary studies.

Achieving SWOT's resolution and accuracy requires rigorous calibration and validation. Potential inaccuracies arising from baseline knowledge, platform motion, electromagnetic signal distortions, and instrument thermal drifts must all be managed by the Ka-band interferometer (Biancamaria et al., 2016). Efforts involving ground-based and airborne calibration, along with in situ campaigns (such as BioSWOT-Med in the Northwestern Mediterranean), will be critical in validating the final data outputs—especially in coastal and highly variable areas.

3.1.3 Strengths and Constraints of SWOT in Coastal/Submesoscale Areas

SWOT significantly reduces the spatial sampling gap inherent in traditional altimetry through its wide-swath coverage. Eddies, filaments, and fronts on submesoscale lengths of a few kilometers (Morrow et al., 2019) are expected to be resolved with this enhanced sampling. Furthermore, the improved revisit cycle aids in studying rapidly changing coastal processes such as freshwater plume dispersion or wind-driven upwelling, which have historically been undersampled by longer-range, nadir-only missions.

Nevertheless, SWOT still faces challenges in coastal areas. Land contamination can weaken the signal near coastlines, particularly when local topography leads to complex radar reflections. Moreover, strong waves, turbulent seas, or atmospheric disturbances can compromise interferometric phase retrieval. The mission's ambitious resolution and accuracy requirements also depend on precise calibration—a task that becomes challenging where wave-current interactions or sharp bathymetric gradients lead to rapidly changing sea states.

It is important to note that SWOT cannot entirely overcome all issues associated with fine-scale coastal dynamics. In some cases, reliable SSH readings near the land-water boundary will still depend on advanced retrackers and coastal-specific post-processing. Nonetheless, the mission's two-dimensional approach, combined with improved orbital parameters and innovative interferometric methods, represents a significant advancement in accurately capturing the core of coastal and submesoscale variability.

3.1.4 Role of MIO and Other Partners in Data Collection

MIO's involvement in SWOT-related initiatives is a prime example of the synergy between regional scientific institutes that provide high-quality ground truth data and mission operators (e.g., NASA, CNES). These collaborations ensure that satellite observations are evaluated and analyzed within the context of local oceanography.

MIO and other European partners also oversee the integration of SWOT data with complementary satellite missions—including Sentinel-3 or Jason-3—and with in situ networks such as Argo or glider fleets. This multi-platform approach is essential for mapping vertical features that cannot be immediately detected by SWOT and for separating true ocean signals from instrument noise (Birol

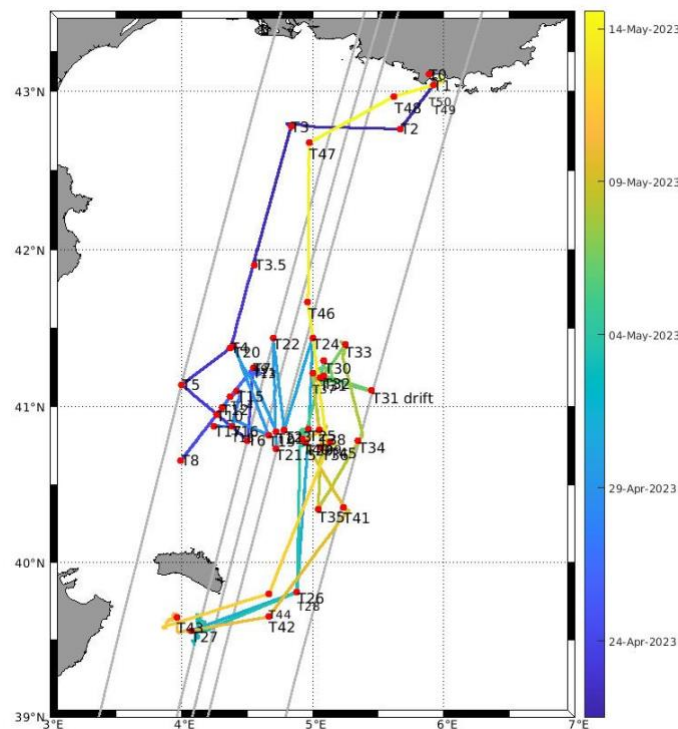
et al., 2017). By combining wide-swath altimetry with other observational streams, scientists can develop a more comprehensive picture of both surface and subsurface dynamics.

Establishing uniform methods for data interchange, quality control, and analysis is one of the primary goals of these collaborations. Stakeholders can access SWOT products, merge them with local in situ observations, and rapidly disseminate results through international data-sharing portals. By accelerating the feedback loop between mission teams and end users, this open-science strategy helps iteratively improve calibration algorithms, product specifications, and observational methodologies (Esteban-Fernández, 2013).

3.2 BioSWOT-Med Campaign

3.2.1 General Presentation of the Field Campaign

The BioSWOT-Med campaign was planned to coincide with anticipated overpasses of SWOT satellite throughout the Northwestern Mediterranean Sea (Doglioli and Grégori, 2023). Its primary objectives were to examine fine-scale phenomena (such as submesoscale eddies and fronts) in both coastal and open-ocean environments and to validate SWOT data products by obtaining high-resolution in situ measurements of oceanographic variables including temperature, salinity, and currents. Employing a mix of ship-based and remote sensing technologies, the campaign sought to close observational gaps that are often encountered near complex coastlines.



*Figura 13. Ship track and station locations of the BioSWOT-Med campaign in the North Balearic Front region. The mission aimed to observe fine-scale processes and validate SWOT satellite data through high-resolution in situ measurements.
Source: BioSWOT-Med campaign [12]*

Designed along several transects in the North Balearic Front region, the campaign sites were chosen for their dynamic circulation, influenced by mesoscale eddy activity (Estournel et al., 2009), river discharges, and the Northern Current. These regions are characteristic of the fine-scale variability found in the Mediterranean, making them ideal testbeds for the improved spatial resolution offered by wide-swath altimetry.

BioSWOT-Med utilized a suite of observational instruments: satellite altimetry from both SWOT and conventional missions (DUACS), autonomous platforms (e.g., gliders), and a dedicated research vessel equipped with the Moving Vessel Profiler (MVP) (Doglioli et al., 2024). The vessel's tracklines were designed to intersect with SWOT ground tracks, thereby allowing simultaneous capture of vertical profiles of temperature, salinity, and density (in situ) alongside satellite-derived sea surface height data. Real-time mapping and data assimilation techniques supported adaptive sampling, guiding the ship toward areas of interest. In fact, the research vessel was directed toward areas with dynamic ocean phenomena—including eddies, filaments, or freshwater plumes—using the SPASSO (Satellite-based Predictions System for ASSimilation and Oceanography) framework (Petrenko et al., 2017). By employing near-real-time satellite altimetry, sea surface temperature, and ocean color data, SPASSO generates predictive maps that highlight potential "hotspots," ensuring that the MVP casts coincide with SWOT ground tracks and capture the most intriguing submesoscale events.

Beyond calibration-validation procedures, BioSWOT-Med provided insights into submesoscale events and related biogeochemical processes in the region. The in situ data collected during the campaign clarified how small-scale structures control vertical mixing, nutrient distribution, and carbon export. These findings are fundamental to the broader goals of SWOT, which aims to revolutionize coastal and inland water monitoring of fine-scale ocean dynamics (Birol et al., 2017).

3.2.2 Moving Vessel Profile (MVP)

Launched from the stern of the research vessel while the ship was in motion, the free-fall “fish” used in BioSWOT-Med—attached by a winch-operated cable—can descend and ascend the water column repeatedly without requiring the ship to stop. Its hydrodynamic design maintains a constant orientation and minimizes drag-induced vibrations, thereby gathering excellent measurements even at modest vessel speeds (Greenan et al., 2003).

Constructed on a robust free-fall body, the MVP combines several oceanographic sensors into a modular payload. Its primary component is a highly precise Conductivity-Temperature-Depth (CTD) module for measuring salinity and temperature. Certain models also incorporate dissolved oxygen probes or optical sensors (fluorometers, transmissometers), thereby extending the instrument's capability to assess biogeochemical parameters. The free-fall design ensures an almost vertical profile and reduces issues related to ship wake.

Depending on mission objectives and local bathymetry, the MVP is released at the surface and allowed to “fall” through the water column during each profiling cycle, reaching depths of several hundred meters. Adjusting the ship's speed—typically between 4 and 8 knots—and regulating the cable length it's possible to control the descent and ascent speeds. Real-time recording of continuous data streams from the CTD sensors onboard enables quick quality checks and preliminary analysis.

Fundamentally, the MVP records depth, salinity, and temperature as a function of pressure (P). From the measured temperature and salinity, seawater density can be calculated using established equations of state (UNESCO, 1981). The computation of dynamic height and geostrophic velocities depends on these density profiles.

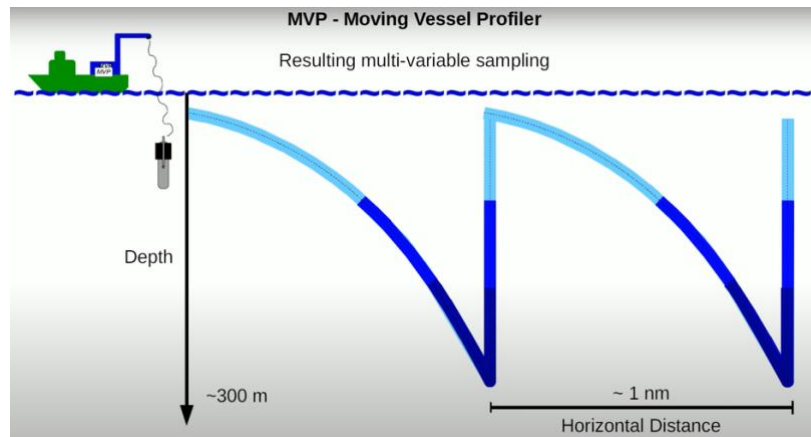


Figura 14. Schematic operation of the Moving Vessel Profiler (MVP), showing repeated free-fall profiles down to ~300 m depth and high-resolution sampling every ~1 nautical mile during ship transit.
Source: Illustration by A.M. Doglioli [13]

Despite its benefits, the MVP has some drawbacks. Rapid depth changes and strong density gradients may affect sensor performance in very shallow or highly stratified waters, potentially causing oversampling or signal delays. Moreover, rough waves can pose operational challenges by increasing cable strain and risking damage to the free-fall fish. High-frequency fluctuations in near-surface layers might also require multiple repeated casts to capture transient phenomena. These limitations necessitate careful planning of sensor calibration techniques, station spacing, and ship speed (Greenan et al., 2003).

The MVP's primary contribution to the BioSWOT-Med campaign was providing high-resolution vertical profiles that coincide with SWOT overpasses. Researchers can validate and refine interferometric altimetry measurements by comparing satellite-derived SSH with in situ steric height calculated from density profiles (Meloni et al., 2019). Additionally, the continuous profiling along ship transects helps identify frontal boundaries and submesoscale features (Rousselet et al., 2019)—an essential aspect of capturing the fine-scale phenomena that SWOT is designed to record.

4. Methods: Data Processing & Statistical Approaches

4.1 Physical computation and data processing

The procedure for managing raw data—both altimetric (SWOT) and in situ (MVP)— and performing key physical calculations is discussed in this part. The ultimate goal is to generate refined datasets and visual outputs proving consistency between satellite and shipboard observations. Building on past research in satellite altimetry (Meloni et al., 2019; Fu and Cazenave, 2001; Chelton et al., 2011) and seawater thermodynamics (McDougall and Barker, 2011), the techniques used here customize existing approaches to the regional setting of the Northwestern Mediterranean.

4.1.1 Data Importation and Setup of Utility Functions

The first step is imports from several python libraries to facilitate scientific computation, data manipulations, and visualisation. Among the most important of these are numpy, scipy, pandas, and matplotlib, which underpin array operations, interpolation, and graphing, respectively. Likewise, the gsw library, Gibbs Seawater, is of essential importance for oceanographic calculations based on the Thermodynamic Equation of Seawater—2010 (TEOS-10) standard (McDougall & Barker 2011). The script also makes use of geopy for geodesic distance calculations, xarray for simplified access to netCDF data, and Basemap for cartographic visualizations.

This code is dependent on a variety of utility functions to get its workflow going. Loadsshuv, as an example, reads netCDF files (SWOT, DUACS) directly with spatial filters. This method is flexible of many data sources, allowing user-defined variable names as well as a file path pattern. Another applies output expression, extract_values, ensures that the pipeline can read MVP outputs by traversing nested arrays, common for MATLAB structures, to extract numerical values.

The helper functions for geometric and vector transformations are rotate_vector and project_vector. These are to orient velocity fields either to analyze motions perpendicular to the transect line, or to compare different components—e.g., total flow vs projected flow. Under various reference frames, these changes can help one understand consistency of altimetric velocity estimates with in situ data (Le Traon and Morrow, 2001).

Separating these core operations into reusable utilities keeps the code modular and reproducible. This design choice also reduces duplicity since the same interpolation or rotation technique can be used at several steps. This sub-step should yield, overall, a robust set of functions to simplify the subsequent loading, filtering, and analysis of data, thereby providing a solid infrastructure for more advanced oceanographic computations.

4.1.2 Loading and Filtering of Altimetric and In Situ Data

Once the utilities are defined, the script loads both altimetric and in situ data. While for altimetry, the filter targets netCDF files that contains variables such as longitude, latitude, sea surface height (SSH), derived geostrophic velocities. Although some geophysical and orbital corrections have already been implemented, the code ensures completeness by filtering NaNs or corrupted entries.

In situ measurements store the MVP data in MATLAB (.mat) files. These, sorted by “plongée” (PL) IDs, contain vertical profiles of temperature, salinity and pressure. Using scipy.io.loadmat, the script extracts arrays for each parameter and any associated metadata such as time stamps and lat/lon positions. At this stage, the code also indicates likely missing or erroneous values.

By applying a geographical filter ($\approx 3^\circ\text{--}6.5^\circ\text{E}$, $38.5^\circ\text{--}44^\circ\text{N}$) we aim to remove data outside the target area, reducing noise contributed by out-of-interest locations (i.e., land or nearby open oceans).

In practice, if a sensor lost contact, or the ship halted sampling for a period of time, in situ profiles may be missing; altimetric measurements are also prone to land contamination or partial coverage (especially near complex coasts). Gradually removing such outlying entries ensures the end dataset is coherent and does not present conflicting data. The expected output is a collection of domain-consistent arrays for spatial interpolation and gridding including valid SSH, ADT, temperature and salinity, and coordinates.

4.1.3 Interpolation on a Regular Grid and Smoothing

Because the MVP data is recorded as discrete casts along the entire path the vessel takes, it is necessary to reformat the data into a continuous, one-dimensional profile so it can be directly compared to swaths from the satellite. The code uses *geopy.distance.distance* to calculate the total distance in the transect, therefore calculating great-circle distances between pairs of adjacent lat/lon. This creates an axis of monotonically increasing distance.

Then, along this distance axis, the script interpolates temperature, salinity, dynamic height (and derived anomalies) to a common 1km grid. Mathematically, it generates y_j at new points x_j , if x_i, y_i are the coordinates (distance, variable) in terms of the original coordinates. Typically, you would use a 1D linear formula:

$$\hat{y}_j = y_i + \frac{(x_j - x_i)}{(x_{i+1} - x_i)} (y_{i+1} - y_i) \quad (10)$$

providing a constant spatial resolution to facilitate direct altimetric data comparisons (Chelton et al., 2011).

Smoothing reduces small-scale noise not characterizing higher-frequency processes beyond the scope of this work or alterations over short-term measurements. For the MVP data in this version of the code, an 11 km moving window is selected as optimal for the filtering of sub-kilometric signals while preserving submesoscale to mesoscale features.

A very important detail are window edges. NaN values result from a partial application of the smoothing window in proximity of the beginning or end of the transect. The code drops these edge points instead of applying any sort of extrapolation. While this shortens the dataset down since it eliminates partial averages, it ensures better quality of the remaining segments. This trade-off sacrifices some coverage for improved integrity of the data.

This yields a set of spaced and smoothed profiles for the MVP's variables. These profiles serve as a refined input for calculating geostrophic velocities and for building side-by-side visualizations with satellite-based ADT measurements.

4.1.4 Calculation of Dynamic Height and Geostrophic Velocities

One of the key elements of the work is to link in situ density fields to ocean currents. The Gibbs Seawater (gsw) library converts observed temperature and salinity to Absolute Salinity (SA) and Conservative Temperature (CT) according to TEOS-10 guidelines (McDougall and Barker, 2011), thus defining the local density, ρ . Once ρ is known, dynamic height (DH), can then be determined by integrating the density anomaly with respect to pressure. This integration is:

$$DH = \frac{1}{g} \int_{p_{\text{ref}}}^p (\rho_{\text{ref}} - \rho(p')) dp' \quad (11)$$

p : pressure; $p(\text{ref})$: reference level (typically the maximum pressure observed in each cast), ρ_{ref} : reference density; g : gravitational acceleration (Gill, 1982).

The GSW function `geo_strf_dyn_height` actually does perform this integration automatically to yield a dynamic height value for each profile. Since every cast (PL) could have a fairly different maximum pressure, the code uses the maximum per cast as $p(\text{ref})$. Centering the resulting dynamic height by subtracting the overall mean—that is, the average of all computed dynamic height values—yields the centered dynamic height:

$$DHC = DH - \langle DH \rangle \quad (12)$$

This centering emphasizes the local anomalies relevant to fine-scale circulation (Le Traon and Morrow, 2001).

However, dynamically derived heights based on in situ profiles are relative and have no absolute reference level. To compare these measurements with satellite-derived data, it is necessary to convert dynamic height into Absolute Dynamic Topography (ADT). This is done by adding an offset from the Mean Dynamic Topography (MDT), which itself is determined as the difference between the geoid and the Mean Sea Surface (MSS). The conversion is expressed as:

$$ADT = MDT + (DH - \langle DH \rangle) \quad (13)$$

In this case MDT provides the needed fixed reference to translate relative dynamic height to an absolute sea surface elevation relative to the geoid. This is necessary to assimilate sparse in situ data with satellite altimetry (Fu and Cazenave, 2001).

The next step is calculating geostrophic velocity with the ADT. The balance between the horizontal pressure gradient and the Coriolis force results in geostrophic flow. The code uses `gsw` to calculate horizontal derivatives of geopotential height (which is proportional to ADT) in a simple 1D (transect) framework. The basic formulas are:

$$u_g = -\frac{1}{f} \frac{\partial \phi}{\partial y}, \quad v_g = \frac{1}{f} \frac{\partial \phi}{\partial x} \quad (14)$$

The Coriolis parameter is given by f , ϕ is the geopotential height (Pedlosky, 1987). Although the study area lies at mid-latitudes—where the Coriolis parameter f does not vary drastically—its spatial variation is still taken into account in the geostrophic velocity calculations.

The code projects the SWOT geostrophic velocity onto the direction perpendicular to the ship's path. An angle is calculated via differences in latitude and longitude between consecutive sites (i and j) along the transect and it's used to adjust the zonal (u) and meridional (v) components. This method produces a SWOT velocity field consistent with the in situ measurement geometry, thus allowing for direct comparisons of derived velocities.

Additionally, the calculation of signed velocities is incorporated to interpret the flow direction relative to the transect. For the SWOT data, the code computes the signed geostrophic velocity—determining whether the flow is directed “to the left” or “to the right” of the transect. (For in situ MVP data, the velocity is inherently measured perpendicular to the transect.) This approach is

useful for locating phenomena like coastal jets or submesoscale filaments, thereby adding directional context beyond the simple magnitude of the velocity.

The final outcome is a consistent set of geostrophic velocity fields derived from in situ dynamic height measurements. These velocities can be further scaled, projected, and visualized alongside satellite-derived ADT velocities to detect fine-scale phenomena and supports the broader objectives of the thesis.

4.1.5 Generation of Output Graphs

The construction of several output graphs illustrating the outcomes of the processing flow is described in this part. Three schematic groups of graphs—each stressing particular aspects of the contrast between in situ MVP data and satellite SWOT products—are arranged below.

Group 1: Map-Based Comparisons

These maps use Basemap projections to visually compare spatial fields and vector fields derived from both datasets.

- Graph 1 (fig. 16): MVP vs. SWOT (ADT-Based Velocity)
A color-coded scatter plot displays the unsmoothed SWOT ADT anomalies, over which quiver plots illustrate the velocity vectors from both MVP and SWOT (computed using ADT). This graph helps assess how well the satellite-derived velocities reproduce the in situ flow patterns.
- Graph 2 (fig. 18): MVP vs. SWOT (TOTAL Velocity)
This map presents the total velocity fields as provided by the SWOT database alongside the MVP measurements. The comparison provides insight into differences arising from various velocity estimation techniques.
- Graph 3 (fig. 19): Projection of SWOT Total Velocity
This plot focuses on the component of SWOT total velocity that is perpendicular to the transect, offering a clear view of cross-transect flows and validating the projection method used for velocity decomposition.

Group 2: Geostrophic velocity Comparisons

These line plots compare the velocity signals along the transect, enabling a direct evaluation of the agreement between datasets

Graph 4 (fig.20): Signed Geostrophic Velocity Comparison

Variables:

- Signed velocities derived from MVP data.
- Signed velocities from SWOT total, from SWOT projected, and from SWOT computed via ADT.
- Additionally, DUACS signed velocity is included for further comparison.

This 1D plot shows the variation of signed velocities along the transect distance, facilitating a detailed analysis of discrepancies between MVP, SWOT (in various processing forms), and DUACS. It is essential for identifying systematic biases or differences in velocity estimation.

Group 3: Additional Diagnostic Plots

These extra graphs provide a deeper understanding of the dynamic topography fields, comparing both the raw and centered (anomaly) values from the different datasets.

- Extra Graph 1: Compares MVP dynamic height anomalies (DHC) with raw dynamic height (DH) alongside SWOT and DUACS centered anomalies and raw topography.
- Extra Graph 2: Focuses on raw dynamic height fields (topography) from MVP, SWOT, and DUACS.
- Extra Graph 3 (fig. 21): Compares centered dynamic topography anomalies across the three datasets.
- Extra Subplots (Graph 4 & Graph 5): Present subplots of the differences between MVP and SWOT, MVP and DUACS, and SWOT and DUACS anomalies.

By grouping the data in different ways, those plots clarify whether discrepancies are due to smoothing, reference-level choices, or intrinsic differences between the data sources. From the raw data to the final geophysical fields, these sets of graphs taken together provide a complete visual validation of the processing chain, proving the general consistency and reliability of the measurements used to interpret ocean circulation dynamics in the study area.

4.2 Aggregated Sensitivity Analysis

4.2.1 Methodology and Physical Rationale

A key goal of this analysis is to assess how the selection of a reference pressure ($p(\text{ref})$) in the in situ dataset influences the relationship between MVP based dynamic height (and thus the derived ADT) and satellite measured ADT (from SWOT). Until now, each PL (plongée) was studied independently. In this approach, the outcomes from several PLs are pooled together to obtain a more reliable estimate of the true $p(\text{ref})$.

In the function `calc_matchup_for_PL` dynamic height (DH) is computed for each PL by integrating the density anomaly from the surface down to the selected $p(\text{ref})$. This can be written as:

$$DH(p) = \frac{1}{g} \int_{p_{\text{ref}}}^p (\rho_{\text{ref}} - \rho(p')) dp' \quad (15)$$

The script loops over a range of possible $p(\text{ref})$ values (from 360 m to 180 m in steps of 10 m), recalculates DHC for each potential $p(\text{ref})$ and compares it against the SWOT product ADT. The premise is that the MVP data might yield a different distribution of anomalies with a slightly different reference level, and that might agree more or less with the satellite altimetry signal.

The matched pairs of DHC and ADT are then used to calculate the *Pearson correlation coefficient*. A high correlation indicates that MVP data match the altimetric signal at that selected reference level.

Speaking about the physical aspect, the $\max(p)$ in each cast is the "level of no motion". In many real-world cases, though, that level may not be completely motionless. However adjusting $p(\text{ref})$ accounts for the fact that some (unknown) baroclinic or barotropic component may be still existent

at depth and contributing to the dynamic height. Thus, doing $p(\text{ref})$ of a range of values helps the code figure out which "no-motion" assumption gives the best overall fit to satellite altimetry.

This study is aggregative, ensuring that any random differences of a single PL (due, e.g., to instruments noise or short time-ocean variability) are diluted while merging results of many PLs (here: PL5 through PL24).

As for the correlation metric itself, it is calculated as:

$$r = \frac{\sum(x_i - \bar{x})(y_i - \bar{y})}{\sqrt{\sum(x_i - \bar{x})^2 \sum(y_i - \bar{y})^2}} \quad (16)$$

where x_i are the MVP-centered DHC values and y_i are the SWOT-centered ADT values. This script loops over the $p(\text{ref})$ candidates and finds the depth that maximizes r (the “optimal reference level”) — that is, where in situ anomalies overlap most strongly with SWOT’s altimetric signal.

4.2.2 Implications of Cross-Validation and Calibration

Finally, upon testing all candidate $p(\text{ref})$ values, the script collates a set of correlation coefficients (averaged across profiles) and determines the optimal depth. This combined outcome constitutes a cross-validation: it employs the satellite altimetry (SWOT) to set up an in situ variable ($p(\text{ref})$).

One might note the paradox that SWOT itself is subject to ongoing calibration efforts. Evens so, for the present analysis, SWOT’s ADT is treated as a sufficiently stable, providing a benchmark for aligning the in situ MVP data. In fact, while SWOT is not a perfect ground truth, the high correlation indicates a consistent physical relationship that can be leveraged to tune the MVP dataset.

The physical impact of changing the reference depth is that it changes the baseline of the vertical integration, shifting the dynamic height anomalies in a way that can either align or misalign with the satellite measurements. Choosing the $p(\text{ref})$ that maximizes this correlation ensures that geostrophic velocities estimated from the in situ dataset are as consistent as possible with the corresponding altimetric fields.

As such, this calibration step increases the integrated dataset's overall reliability, especially for fine-scale or near-coastal circulation studies, where even a slight mismatch in reference-level assumptions could alter the interpretation of submesoscale structures.

4.3 Scatterplot Comparisons & Statistical Summaries

4.3.1 Selection and Interpretation of Statistical Metrics for Cal/Val

In this section, we detail the statistical metrics selected to assess and validate our aggregated analysis across all PL values (ranging from 5 to 24). Two datasets are considered: one where DHC MVP is compared to ADT SWOT using the non-optimized reference— $p(\text{ref}) = p(\text{max})$ — and another where the optimal candidate is selected— $p(\text{ref}) = p(\text{optimal})$. The metrics chosen provide complementary insights into the model’s calibration. Below, each metric is defined and its role within the paper is explained.

RMSE (Root Mean Squared Error):

Definition: RMSE is the square root of the mean of the squared differences between the predicted and observed values.

This metric quantifies the average error magnitude between ADT MVP and ADT SWOT. It is crucial for assessing the overall accuracy of the model calibration, as lower RMSE values indicate a better fit of the predictions to the observed data.

Pearson r (Pearson Correlation Coefficient):

Definition: Pearson r measures the strength and direction of the linear relationship between two variables, with values ranging from -1 (perfect negative correlation) to +1 (perfect positive correlation).

This statistic evaluates the degree of linear agreement between ADT MVP and ADT SWOT. A high positive Pearson r confirms that the model predictions closely follow the trend of the observed data, which is essential for validating the model's consistency.

Slope (of the Regression Line):

Definition: The slope is the coefficient obtained from linear regression, representing the rate of change in DHC MVP with respect to ADT SWOT.

A slope close to one suggests that the two measures change proportionally. Deviations from one indicate a systematic bias in the scaling between ADT MVP and ADT SWOT. This metric is used to detect and quantify such biases, thus informing adjustments in the calibration process.

Standard Deviation (Std MVP and Std SWOT):

Definition: Standard deviation is a measure of the dispersion or variability of data points around the mean value.

The standard deviations of DHC MVP and ADT SWOT provide insight into the spread within each dataset, giving a hint about the instruments' ability to capture variations in the observed data.

The comparison between the two datasets allows us to assess the impact of optimization on predictive accuracy while also providing statistical measures that can be interpreted independently of the p(ref) selection.

4.4 Spectral & Coherence Analysis

4.4.1 PSD Estimation and Ensemble Averaging

Each dataset is divided into continuous segments, which excludes long stretches of missing or invalid data before computing the Power Spectral Density (PSD). In the specific code utilized, this step is realized through the `split_on_nan` function that verifies a defined threshold (`max_consecutive_nans`) of consecutive NaNs to proceed with partitioning. This makes sure that discontinuities resulting from sensor drop-outs or gaps in the interpolation, do not introduce spurious low-frequency energy in the final PSD. Consequently, each segment contains a sufficiently continuous signal where it is suitable for unbiased spectral estimation.

The PSD for each continuous segment is computed using Welch's method (Welch, 1967). In particular, a Hann window is applied to reduce spectral leakage across segment boundaries, while the frequency resolution is specified by the `nperseg` command (number of data points per segment). To increase the sample size, the method also applies overlapping windows of 50%, therefore each segment shares half of its data points with the previous segment. Windowed and overlapped

averaging of the FFT, as described by Emery and Thomson [2001], provides a smoother and statistically more robust way of estimating the corresponding PSD than a direct FFT.

When dealing with shorter segments (less than 10 data points) the psd is not computed, as FFT-based estimation is not possible and would lead to high variance. This filtering step is particularly important in oceanography, since short tracks can introduce a bias in spectral slope by artificially enhancing high-frequency components.

After computing the PSD for each segment, we average all of the estimates to obtain an ensemble averaged estimate. This is accomplished by interpolating each segment's PSD to a common frequency grid and averaging over all segments. The `ensemble_average_psd` function combines multiple independent segments into a single and robust PSD estimate.

The PSD values expressed in $\text{m}^2/(\text{cyc}/\text{km})$ are subsequently rearranged to $\text{cm}^2/(\text{cyc}/\text{km})$ by applying a simple scaling factor of 10^4 on the averaged data. This conversion allows for direct comparison with studies that present SSH variance on centimeter scales. Although the value of dimensionless power-law slopes (e.g., -2 , -3) are invariant under unit conversions, it's important to choose units such that they facilitate comparisons to spectral ranges widely reported in the literature (e.g., Le Traon et al., 2015).

Spectral slopes are estimated by fitting log–log linear regressions to the ensemble-averaged PSD as part of the analysis. The function `loglog_regression` fits a power law according to a regression of $\log(P)$ vs. $\log(f)$ in the form $P(f) \propto f^m$. Spectral slopes in oceanography are usually between -2 and -3 at the mesoscale-to-submesoscale transition (e.g., Callies and Ferrari, 2013). Any deviations from these theoretical slopes may be attributed to ageostrophic processes, mesoscale eddy, or instrument noise.

Each PSD estimate, which includes MVP (in situ), SWOT, and DUACS, is calculated separately and plotted together. These datasets are complementary: MVP is the only in situ coverage of dynamically height variability; SWOT and DUACS altimetry data represent two products from satellite platforms sampling different spatial resolution. This comparison allows the assessment of how well the satellite measurements reproduce the in situ spectrum over scales and, simultaneously, identify noise floors or instrument-related artifacts.

4.4.2 Coherence Computation and Technical Challenges

To expand on the PSD analysis, we calculate spectral coherence (0 to 1)—a measure of the degree to which two signals vary in a consistent manner at each frequency. Assessing the function `split_on_nan_pair`, which, as its name suggests, processes 2 datasets (i.e.: MVP and SWOT) at the same time, forcing only the intervals in which both signals have a sufficient amount of good data. This avoids an artificial increase in coherence due to interpolation over long gaps in one of the datasets.

Once segmentation is done, Welch's method is used to calculate the magnitude-squared coherence C_{xy} between two signals, defined as:

$$C_{xy}(f) = \frac{|G_{xy}(f)|^2}{G_{xx}(f)G_{yy}(f)} \quad (17)$$

$G_{xy}(f)$ is the cross-spectral density of the signals x and y , and $G_{xx}(f)$ and $G_{yy}(f)$ are their auto-spectral densities. The overlapping window procedure and Hann windowing are preserved to help reduce variance in the coherence estimate (Bendat and Piersol, 2011).

Noise of each measurement platform can diminish high-frequency coherence between the altimetric and in situ signals. Coherence estimates are further complicated by differences in sampling strategies (along-track altimetry vs. discrete casts). This method averages multiple profiles by segmenting them, and highlights regions that consistently show high (or low) coherence values, aiming to reduce and contextualize random noise within the data.

Estimates of final coherence gives insight in how well each satellite product agrees with in situ data at varying scales. In the case of mesoscale frequencies, high coherence suggests that SWOT or DUACS captures the same structures as the MVP, while at finer scales reduced coherence may reveal a need for higher resolution or improved noise filtering techniques. Finally, coherence is included in the same figure as the PSD, allowing simultaneous evaluation of the distribution of spectral energy and coherence.

5. Results and Discussion

5.1 ADT Comparison and Velocity Fields

5.1.1 Graphical Presentation of ADT and Velocity Fields

Here, we show and thoroughly discuss the main visual outputs resulting from the SWOT altimetric products and in situ MVP dataset comparison. The aim is to connect the nature of each graphic to the underlying physical processes, especially the relative magnitude of geostrophic currents and the occurrence of submesoscale phenomena like cyclonic or anticyclonic eddies.

While all profiles from 5 to 24 were analyzed (*Figure 15*), profile 12 was selected for a more detailed illustration of the key features, as it is particularly representative and clear. In the aggregated statistical analysis that follows, we will observe that the characteristics seen in profile 12 are representative of what is observed across all profiles.

The first three maps all use the same visual framework (*fig. 16, 18, 19*). In each plot, the background color shading illustrates SWOT-derived Absolute Dynamic Topography (ADT) at the sea surface, back-projected to a geographic basemap of our Northwestern Mediterranean study region. The color scale (from -0.10 m to $+0.10$ m) denotes positive (warm colors) or negative (cool colors) sea levels relative to the regional mean. On each of these maps are three main features: the MVP transect, which is a ship-based sampling track shown as a continuous black line extending across the domain; a frontal boundary (colored in purple), separating the biological region identified based on concurrent data; and velocity vectors, comparing the current estimates from the satellite SWOT to in situ geostrophic currents calculated from MVP dynamic height (DHC).

The maps (*fig. 16, 18, 19*) plot velocity vectors which enable the direct inter-comparison of altimetric and in situ flow estimates. There are two groups of velocity vectors in these figures:

1. SWOT-based velocity (e.g. in blue or green), determined directly from ADT gradients or given in the SWOT product.
2. MVP-based velocity (red), using the gradient of the dynamic height anomaly (DHC).

These vectors can clarify small but prominent distinctions in magnitude and direction, particularly where local processes—ageostrophic currents, coastal contamination or submesoscale filaments—complicate the satellite retrievals (Le Traon & Morrow, 2001).

In this subsection, each of the figures is introduced in turn, providing a close reading of the oceanic processes they capture.

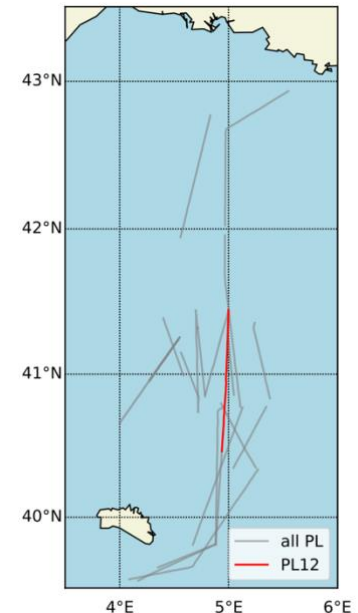


Figure 15. Map of MVP transects conducted during the BioSWOT-Med campaign. Transect PL12 is highlighted in red, while the remaining transects are shown in grey.

Source: Bessi re, [8]

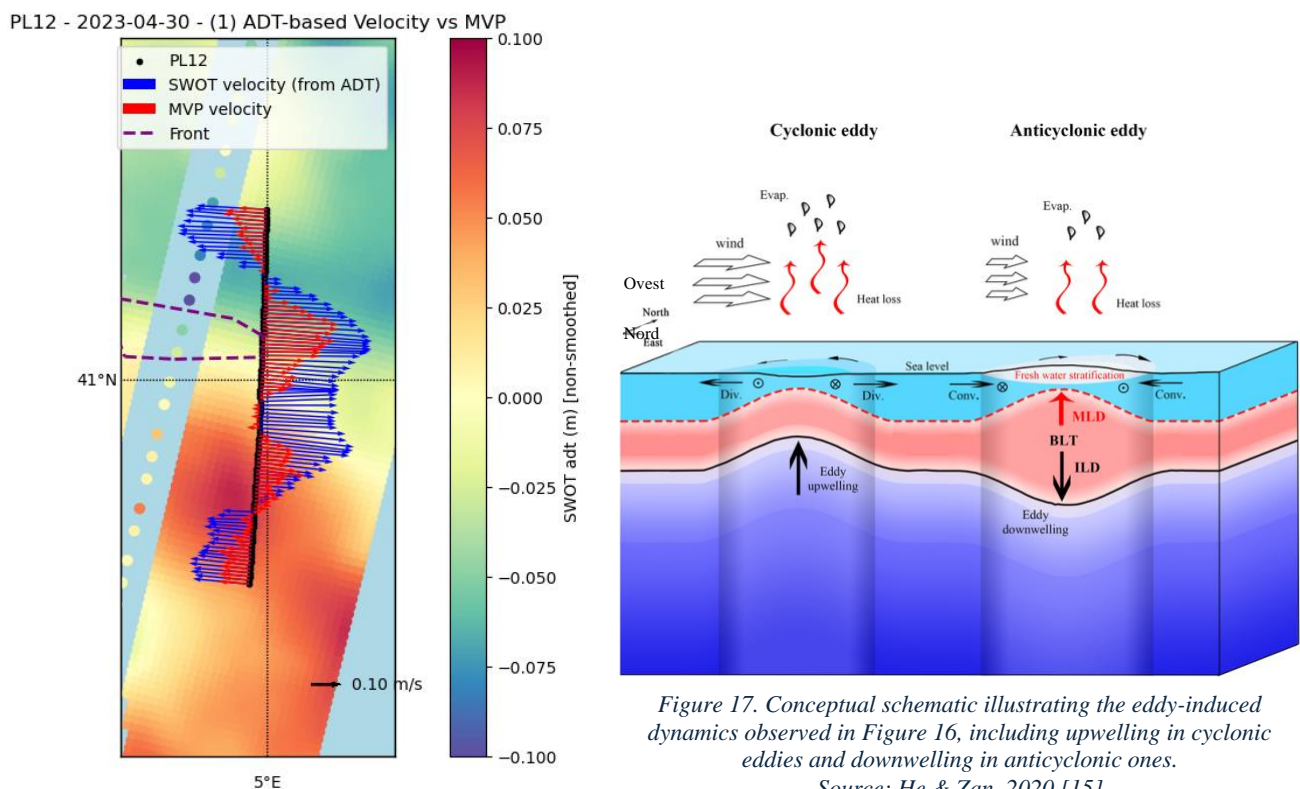
Figures

On the background of *Figure 16* we have two sets of velocity vectors;

1. Blue vectors reflect the geostrophic currents calculated directly from the SWOT ADT gradients.
2. Red vectors are the velocities obtained from MVP dynamic height (DHC) observations, following a smoothing window (11km) applied to filter out high frequency noise.

The comparison of the ADT field (SWOT) and the in situ dynamic height fields shows how well aligned these datasets are. The red velocity vectors (MVP) strengthen or change character rapidly along the region DHC where a nearly vertical slope is present, while the blue altimetric vectors take on a similar behavior though with larger magnitudes. The near-matching of both datasets implies that the large-scale geostrophic signal is both present and robustly captured.

Cyclonic (or anticyclonic) circulations are seen as ADT highs (or lows) rotating around the centre in some parts of *Figure 16*. A cyclonic eddy, for example, is identified in the top-left edge of the domain where color shading drops to negative anomalies (dark blues), with velocity arrows spinning counterclockwise. On the other hand, an anticyclonic eddy could appear, with positive ADT anomalies (oranges/reds) and clockwise whirl in the arrow field. Both SWOT and MVP velocity directions show similar coherent vortex structures indicating a geostrophic current about the eddy core confirmed in this region. However, discrepancies are apparent; yielding vectors that differ from the in situ data by $\sim 0.2\text{ms}^{-1}$.



The following figure (*fig. 18*) substitutes the ADT-derived geostrophic velocity from SWOT with the so-called DB velocity fields ($u_{gos} + v_{gos}$), delivered directly from the SWOT product. Specifically, color scale for the background remains the ADT anomaly, however, the SWOT-derived DB velocities are not constrained to be perpendicular to the ship transect, thus offering a more complete representation of surface flow. For consistency, MVP vectors keep red coloring.

In the case of *Figure 18*, it is not appropriate to compare the total geostrophic velocities from SWOT directly with those from MVP because they measure fundamentally different quantities. By definition, the MVP is constrained to produce perpendicular velocity vectors, while SWOT offers a full 2D view. Instead, the key insight from the figure is whether the velocity vectors point in the same direction—that is, whether they share the same sign. In most parts of the transect, both instruments show strong agreement in vector orientation, confirming a similar flow pattern. The only notable exception is a section near the middle where the vectors from SWOT and MVP point in opposite directions.

The third figure (*fig. 19*) examines cross-transect components, projecting SWOT's full velocity perpendicularly to the MVP line. In regions where a significant cross-front velocity is present (e.g., outflow from a coastal current or a filamental penetration), the green (SWOT) and red (MVP) arrows should be directed in the same direction and sign.

From observing *Figure 19*, it is often found that the sign of the large-scale sign (positive or negative) matches, but the amplitude can differ. For example, -cross-transect flows of $+0.15\text{ms}$ in MVP will be rendered as $+0.30\text{ms}$ in SWOT. This indicates that the altimeter derived data may be overestimating the cross-frontal shear or, alternately, that MVP smoothing has washed out velocity peaks. In addition, such comparisons can reveal submesoscale filaments along the front: on a steep ADT decrease, the shading might indicate a narrow band of increased cross-transect flow, which would correspond to the localized source or sink of water masses.

Line plots (*fig. 20*) that capture how unique velocity estimates change along the distance axis of the MVP transect (the horizontal axis of the MVP

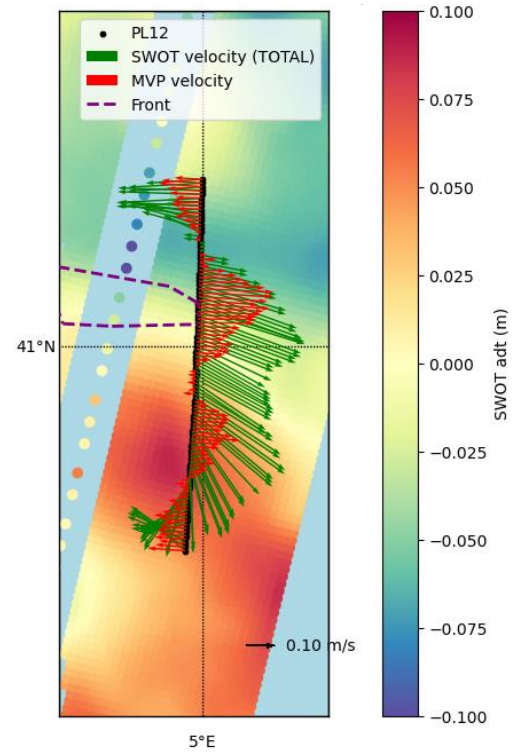


Figure 18. Comparison between SWOT database-derived surface velocities (green) and MVP velocities (red) along transect PL12.
Source: Author's own processing

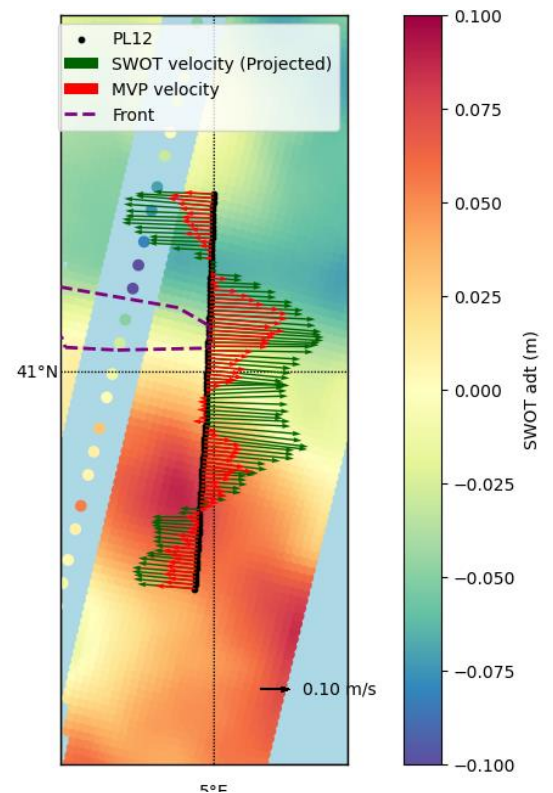


Figure 19. SWOT (green) and MVP (red) velocity vectors projected perpendicularly to transect PL12.
Source: Author's own processing

transect, as depicted on the map-based figures) are an important counterpart to the map-based figures. Some line might show MVP's signed geostrophic velocity, others:

- SWOT DB (total and projected respectively)
- SWOT ADT-based (based only on ADT gradients)
- DUACS (for comparison with another altimetric product)

By scanning from left to right, the reader sees how well or poorly each dataset matches. Steep peaks (e.g. from $+0.2\text{ms}^{-1}$ to -0.1ms^{-1}) may suggest crossing an eddy edge or some strong frontal region.

Head-to-head comparison line plots shows that MVP velocities are systematically lower than the SWOT curves. For example, at 20–35 km, the difference is $\sim 0.05\text{ m s}^{-1}$, then developing through the next kilometers of the transect to a delta of $\sim 0.30\text{ m s}^{-1}$ at the maximum. Between 40–50km, one notes that the DUACS line falls with the MVP line, as it also captures a weaker signal. These characteristics support the idea that the satellite-based total velocity may be systematically high, perhaps due to unresolved ageostrophic effects or miscalibration of an MDT. The line plots additionally illustrate the regions of good agreement, which are critical to test the synergy of in situ and altimetric data. Additionally, a separate 1D figure (fig.21) might focus on ADT anomalies themselves, showing how strongly the two fields co-vary.

PL12 - (4) Signed Velocity Comparison (MVP, TOT, Projected, ADT-based, DUACS)

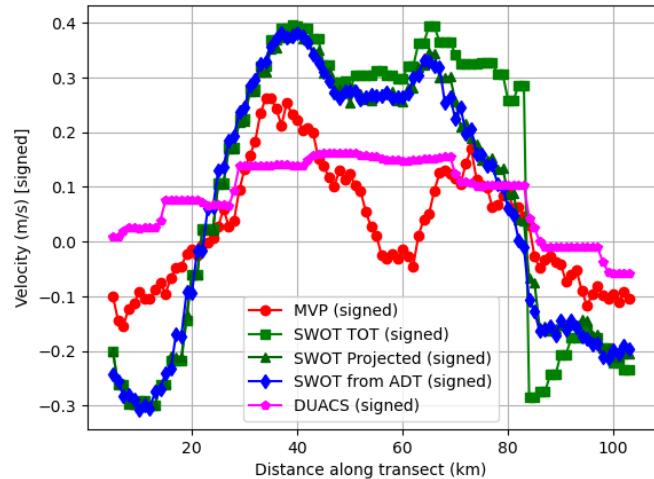


Figure 20. Comparison of signed geostrophic velocities (MVP, SWOT TOT, SWOT projected, SWOT ADT-based, and DUACS), highlighting steep peaks that may indicate eddy boundaries or strong frontal regions.

Source: Author's own processing

PL12 - Grafico 1 (extra): Confronto anomalie centrate e topografie grezze

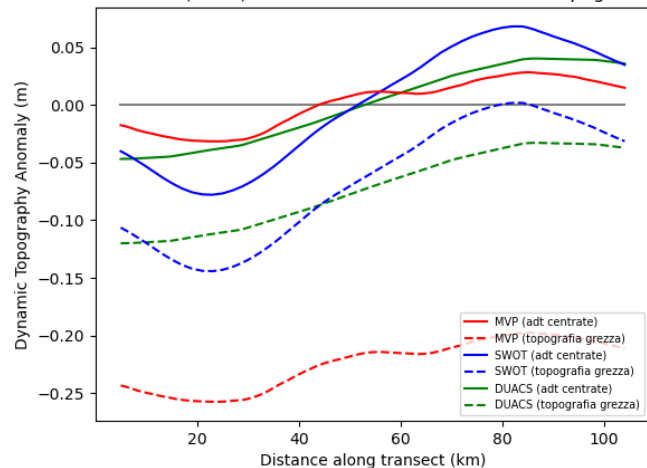


Figure 11. Comparison of dynamic topography anomalies (MVP, SWOT, and DUACS), illustrating how both raw and centered values vary along the transect.

Source: Author's own processing

5.1.2 Integrated Discussion and Comparative Analysis

Here we synthesize the interpretations to summarize the oceanographic features present—focusing specifically on frontal boundaries, eddies, and potential submesoscale filaments—and highlight the key similarities and mismatches between SWOT & MVP.

For all cases the purple polygon marking the front is tightly coupled to the sharp gradients in ADT and MVP dynamic height. In map view, as shown in *Figures 16, 18 and 19*, we observe a tight cluster of elevated velocity vectors immediately ahead of this front, indicative of a strong cross-frontal geostrophic current. The profiles (*Figure 4*) confirm that velocity magnitudes around the front's latitude are generally in the $\sim 0.2\text{--}0.3\text{ms}^{-1}$ range, about 50% above those in the neighboring waters. This strongly suggests that the front represents not only a boundary between distinct water masses (biologically identified), but also an energetic boundary with substantial lateral flux.

Map-based SWOT ADT field hosts cyclonic and anticyclonic eddies (for example, deep-blue swirl: cyclonic rotation; red/orange zone: anticyclonic). Also, these eddies are similarly manifest in the altimetric ADT suggesting that SWOT is capturing the central vorticity structure fairly well at the mesoscale (tens of kilometers). At submesoscale ($\sim 1\text{--}10\text{km}$), however, the line plots in *Figure 20* may capture short-wavelength fluctuations in MVP velocity that are not as clearly present in the velocities from SWOT DB or ADT. This mismatch may suggest that the satellite swath filtering, or the basic altimetric corrections, smooths out smaller eddy edges or filaments.

The vertical profiles of temperature, salinity, and density (*fig. 22*) provide additional support for these features, showing the typical upwelling of cyclonic eddies and downwelling of anti-cyclonic eddies. The representative practical salinity and potential density panels capture these anomalies and mirror the eddy structures observed in the altimetric fields, validating the mesoscale structure and circulation inferred from MVP data.

One consistent finding, evident in vectors lengths of *Figures 16, 17, 18* and confirmed by line plots of ADT in *Figures 20 and 21*, is that SWOT TOT velocities are typically greater than MVP's over regions with high ADT gradient. One of the likely culprits is the MDT (mean dynamic topography) offset applied in altimetric processing. If the baseline MDT is slightly too low (or too high) with respect to what is happening in reality, then the local anomaly (SLA) will be overestimated (also) leading to a slope in the altimetric product that is excessive. Alternatively some baroclinic or inertial motions are being partially captured in the altimetric solution but do not exactly correspond to the geostrophic assumption under which MVP's dynamic heights are calculated. Overall, the additional projected vector continues to confirm that total vectors are less consistent than cross-transect velocities.

SWOT's total velocity leads one to wonder just how much ageostrophic flow the altimeter really resolves. In some situations, such as during strong wind events or over the continental shelf, wind

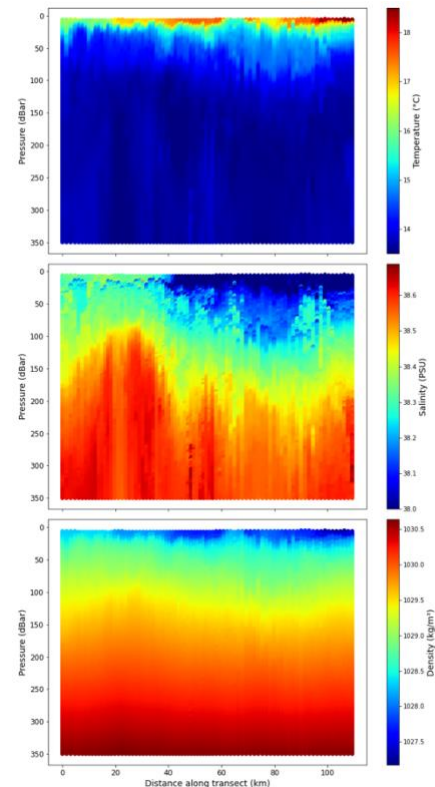


Figure 22. Vertical sections of temperature, salinity, and density along the MVP transect. These profiles confirm the alignment of dynamic height anomalies with the front, indicating strong lateral flux and energetic mesoscale to submesoscale features (e.g., eddies and filaments).

Source: Bessi re, [8]

driven currents or crossover topographic steering that is non-geostrophic may occur. On the other hand, the MVP only calculates geostrophic velocity from steric height. So ageostrophic flows might account for part of the altimeter's higher velocity. But the mosaic of results suggests that the difference is more consistent, indicative of an overall bias rather than episodic wind-blown bursts.

Out-of-place velocity vectors present within some SWOT fields (even preferentially reversed in orientation with respect to MVP) are observed. These mismatches highlight the already established difficulty in recovering usable altimetry in coastal regions.

By going across the four figures:

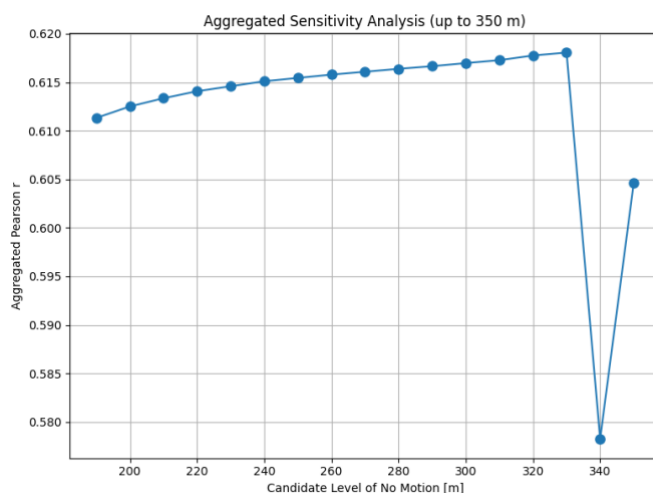
- Regions of strong positive agreement: regions with large mesoscale eddies or fronts can contribute to important but quite smooth ADT gradients. Here, line plots depict the $<0.05\text{ms}^{-1}$ difference between the SWOT TOT and MVP velocities.
- Weak agreement regions: Short-scale filaments near the front. Differences can spike to 0.3 m s^{-1} , and altimetric ADT anomalies can be out of phase compared to MVP.

The detailed breakdown of the graphical evidence points to a generally good match of SWOT altimetry and MVP in situ competitor measurements at scales larger than $\sim 10\text{km}$. But the residual errors (which could arise from MDT offsets, smoothing, or partial ageostrophy) illustrate the care that must go into interpreting SWOT velocities in frontal regions and submesoscale eddy fields. The following sections take quantitative measures based on the observations utilizing scatterplots, correlation coefficients and spectral coherence to link these visual observations with statistical evidence. All in all, these results present a key advancement in refining the calibration of SWOT products and in our capability to capture fine-scale oceanographic features in the Northwestern Mediterranean.

5.2 Sensitivity Analysis

5.2.1 Graphical Presentation of the Aggregated Sensitivity Analysis

The chart in *Figure 23* plots the Pearson correlation coefficient (vertical axis) as a function of a “candidate level of no motion” (horizontal axis, in meters). Every dot on the graph is therefore the averaged correlation output of assigning a reference pressure ($p(\text{ref})$) for no-motion at different depth levels (from around 180m to 350m here). Finally, it combines all MVP–SWOT matchups along all transects (PL5 to PL24) and computes a single Pearson r for each candidate of $p(\text{ref})$.



*Figure 23. Aggregated Sensitivity Analysis plotting the median Pearson correlation (vertical axis) versus the candidate level of no motion (horizontal axis, in meters).
Source: Author's own processing*

- Horizontal axis (candidate no motion level [m]). In the range of values (from roughly 190m up to 350m), the code recomputes the geostrophic velocities under the assumption that there is effectively zero flow at that chosen depth, then aggregates the correlation with SWOT's ADT fields.
- Vertical Axis (Median Pearson r Aggregated). The correlation values (low end at approximately 0.58 high end up to around 0.62) reflect a moderate agreement level between in situ and SWOT altimetric measurements. Shifts in r on the order of hundredths (e.g., 0.610 to 0.618) are still important in the field of submesoscale oceanography, where the noise of measurements generally restrict stronger correlations.

The graph indicates an almost increasing trend from ~190m till ~330m, where we find the correlation increases from $r=0.610$ to its peak ~ 0.618 . After 330 m, there is a sudden drop at 340 m—where r plunges below 0.58—followed by a partial rebound near 350 m. Affected by this drop at around 340m, is the clear “spike” (inverted peak) feature on the curve suggesting there might be some sparsely populated data at that depth (which we are now able to detect) or some computational abnormality in the matchup procedure.

The higher Pearson r is achieved at 330m, with $r \approx 0.618$, as reported in the figure caption. This designates 330m as the “optimal reference depth” for no motion given all available data, meaning that referencing the dynamic height calculations to 330m results in the best overall correlation (on average) between MVP-based steric height and SWOT altimetric ADT.

5.2.2 Integrated Discussion: Implications for Reference-Level Selection

In oceanography, the selection of a “level of no motion” ($p(\text{ref})$) is a standard step in converting temperature–salinity (T–S) profiles to dynamic height (Gill, 1982). This assumption also implies that the flow velocity at or below a certain depth is negligible, which is generally accepted as valid for deep isopycnal layers in relatively stable regions. Nevertheless, even within the Mediterranean basin, the mid-depth may exhibit substantial spatial heterogeneity, yielding a difficulty in choosing a no-motion reference that would be homogeneous in space (Millot & Taupier-Letage, 2005). Accordingly, an aggregated correlation-based approach is employed to determine the depth that best matches in situ data to altimetric fields in the global sense.

The increase in Pearson's r from approximately 190 m to 330 m is monotonic, suggesting that moving deeper yields better agreement between the geostrophic calculations and the SWOT altimetric signal. However, the last two points in this figure may be unreliable because only a small number of casts reach those depths, effectively introducing noise. Within the reliable range—where sufficient data are available, as indicated by the smooth portion of the curve—this rise in r at greater depths implies that the level of no motion is likely deeper than 330 m, and that extending casts even further could further improve the match. This finding supports the idea that the baroclinic structure above ~330 m is the most relevant for the dynamic height, while below this depth the water column becomes much more homogeneous. Adopting a no-motion assumption at deeper levels could lead to a more realistic geostrophic velocity at the surface.

While an r of 0.618 is not very high per se, submesoscale ocean processes and measurement limitations (particularly in the nearshore zone) usually constrain correlations in the 0.60–0.70 range (Le Traon & Morrow, 2001; Morrow et al., 2019). The same 0.618 in many transects demonstrates a coherence between the altimetric ADT anomalies and the dynamic heights derived from the MVP that is not random. It confirms that a deeper reference level (~330m) is indeed more appropriate for capturing the principal geostrophic signal across the NW Mediterranean sampling grid.

The reason for which 330m is “optimal” is pivotal for the whole calibration–validation chain (Refer to Section 4.2 also, where the algorithmic methodology was explicated). Recomputing the geostrophic fields based on the MVP geostrophic fields but using this no-motion depth could improve the coherence between in situ and satellite observations when analysing fronts, eddies, and submesoscale structures (Sections 5.1 and 5.3).

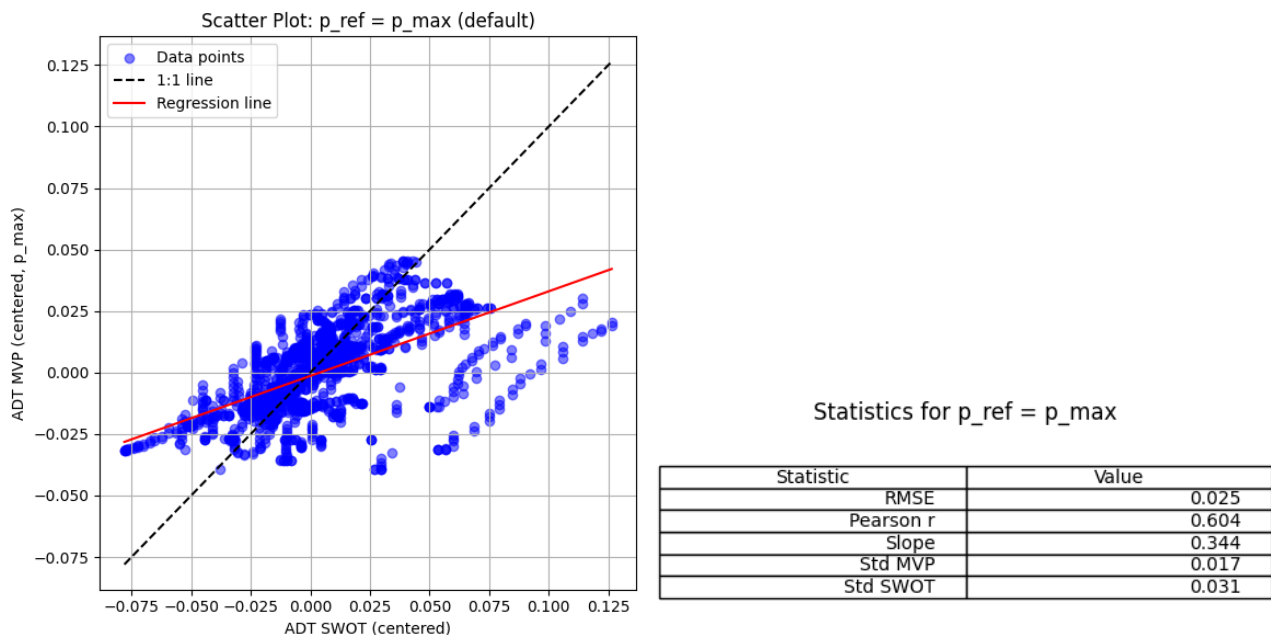
This will provide context for our later comparison of altimetric and in situ measurements, especially in light of the more detailed statistical metrics (RMSE, correlation, slope, etc.) discussed in 5.3.

5.3 Statistics

5.3.1 Presentation of Scatterplots and Statistical Summaries

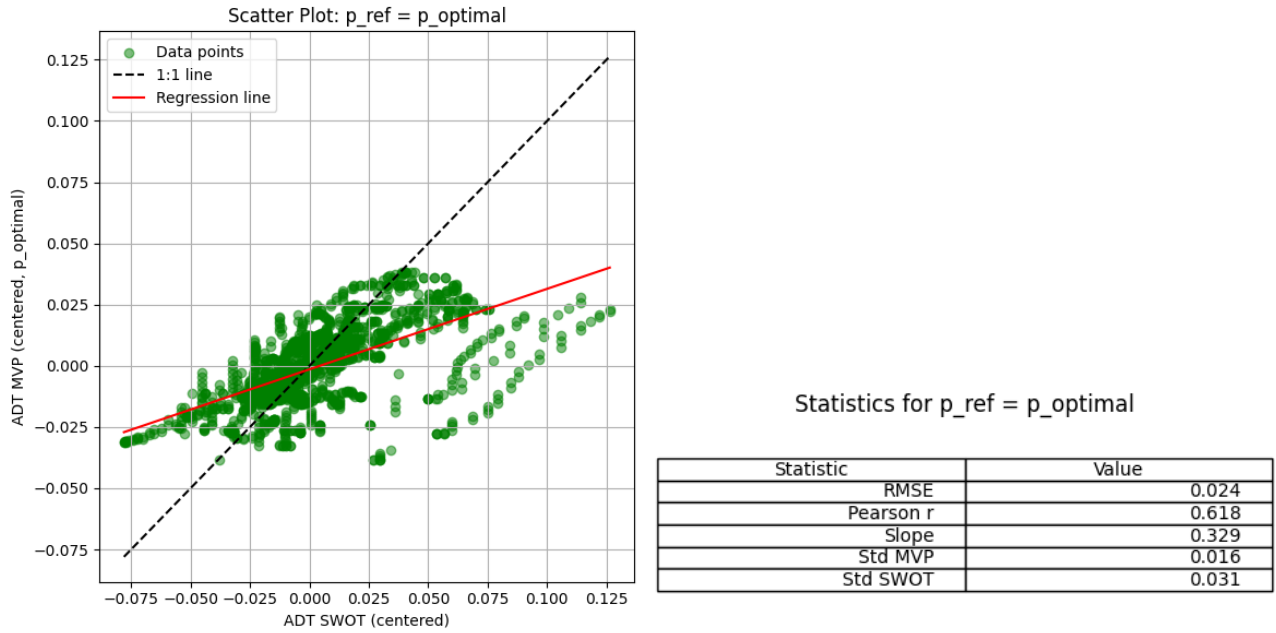
The two scatterplots in *Figures 24 and 25* show the relationship of the SWOT altimetric ADT (horizontal axis; centered by subtracting the mean) and MVP-determined ADT (vertical axis; same centering). However, although both are derived from all transects' MVP profiles, they differ with respect to the assumed reference pressure at which MVP dynamic height is computed ($p(\text{ref})$):

1. *Figure 24*: $p(\text{ref}) = p(\text{max})$. The first plot (blue dots) is based on the classic technique of being no motion level at maximum measured depth per profile.



*Figure 24. Source: Scatter plot (blue points) for $p(\text{ref})=p(\text{max})$, paired with its performance table.
Source: Author's own processing*

2. *Figure 25: $p(\text{ref}) = p(\text{optimal})$.* The second plot (green dots) is an application of the optimal reference depth ($\sim 330\text{m}$, calculated in Section 5.2) on the entire dataset.



*Figure 25. Scatter plot (green points) for $p(\text{ref})=p(\text{optimal})$, paired with its performance table.
Source: Author's own processing*

Both charts display:

- A 1:1 line (dashed black) of perfect agreement between the MVP and SWOT.
- A linear regression line (red), whose slope and intercept quantify the dependence of the MVP DHC on altimetric ADT in practice.

The points in each scatterplot take the shape of a cloud that is roughly elliptical, oriented bottom-left to top-right of the graph, indicating a strong positive correlation ($r > 0.60$) between the two datasets. The general trend is upward, indicating that as MVP DHC (positive anomalies) increases, SWOT ADT also tends to increase, though the relationship is not perfectly 1:1. The vertical dispersion around the regression line reflects to some degree the nature of smaller-scale or nearshore signals that differ between MVP (which resolves steeper baroclinic gradients in a way that SWOT cannot) and SWOT (influenced by the mean dynamic topography). In ADT space, a subset of points near $(-0.075, -0.025)$ (i.e., both x and $y < -0.025$) implies that a higher amplitude of negative anomalies in MVP data occurs in some segments of the transects. These probably represent submesoscale eddies or local front intensification not equally represented in the satellite fields (Morrow et al., 2019). Here are the main metrics considered for the two reference depth choices:

- For $p(\text{ref}) = p(\text{max})$: $\text{RMSE} \approx 0.025$, $r \approx 0.604$, slope ≈ 0.344
- For $p(\text{ref}) = p(\text{optimal})$: $\text{RMSE} \approx 0.024$, $r \approx 0.618$, slope ≈ 0.329

Although the RMSE and slope differences are minimal, the change in correlation (0.604 to 0.618) is significant. That is, using a uniform deeper reference pressure smoothes out random variations in ADT and results in better matching with SWOT data on average over all transects (see also Le Traon & Morrow, 2001).

MVP standard deviation (~ 0.016) remains smaller than SWOT's (~ 0.031) for all time frames. Physically, this suggests:

- MVP is doing some sampling along a single ship track, along with some local constraints and smoothing. Short-scale extremes may be suppressed by the 11km filtering used for MVP, resulting in lower variability (McDougall & Barker, 2011).
- SWOT looks over broader swaths (and may capture both baroclinic and ageostrophic signals), hence higher variance.

5.3.2 Discussion: Statistical Insights and Relevance to the Study

Comparing the default $p(\text{max})$ to the optimal ~ 330 m reference depth, the Pearson correlation improves (0.618 vs. 0.604) and the RMSE is marginally lower (0.024 vs. 0.025m). Though small in absolute terms, these improvements represent more consistent alignments across multiple transects. Since every PL may feature unique oceanographic structures, a 0.01m decrease in RMSE can be significant on submesoscale fronts or eddy margins, where altimetric error can hide physical variability.

The fact that for $p(\text{ref})=p(\text{max})$ the slope is 0.34 and for $p(\text{ref})=p(\text{optimal})$ the slope is ~ 0.33 suggesting that in general MVP anomalies tend to be of significantly lower amplitude than their SWOT counterparts (1:1 slope would be 1.0). The underestimation in MVP might instead result from local smoothing, or from incomplete capture of dynamic processes above the deepest reference. It may also signal overestimated slopes in the altimetric ADT when the mean dynamic topography correction (MDT) has imperfections.

An RMSE of approximately 0.024–0.025 can be interpreted in the context of physically reasonable altimetric uncertainties: most submesoscale signals will center on sea-level displacements in the few-centimeter range, meaning that a root-mean-square difference of 2–3 cm is large but not extraordinary. In coastal or topographically complex regions, altimeters are often contaminated resulting in 2–5cm of residual errors (Morrow et al., 2019). So, the results here are in plausible ranges and show that additional calibration could reduce these gaps.

The std dev for the MVP is ~ 0.016 . The reduced dispersion indicates that the MVP transect is not picking up such extreme outliers or that the smoothing window is suppressing fine-scale “spikes”. Another possibility is if the partial sampling path left out highly dynamic zones computed earlier in the domain. The std dev for SWOT is ~ 0.031 ; the extensive spread relates to the extensive coverage.

These scatterplots and statistics verify that the deeper reference levels $p(\text{optimal})$ improve the overall synergy of the MVP in situ measurements with the SWOT altimetric ADT, which concurs with the aggregated sensitivity results from Section 5.2. For submesoscale studies, where the noise associated with measurements and imperfect geophysical corrections hinders higher correlations (Le Traon & Morrow, 2001), the correlation of ~ 0.62 is modest yet acceptable. The standard deviation contrast further illustrates that remote sensing captures a wider spectrum of anomalies than in situ transect-based data that remains more focal.

This statistical comparison provides the basis for additional analysis in Section 5.4 of spectral analysis and coherence. If offsets are consistently identified (e.g., slope ~ 0.33), this suggests that calibrations could be needed to make altimetric ADT more representative of the coast or to be adjusted to account for any residual baroclinic signal not retained in the selected reference. These

gradual enhancements in correlation, RMSE and slope ultimately correspond to a more accurate representation of mesoscale and submesoscale processes in the area of study.

Based on the comparison above in terms of statistics, Section 5.4 further analyzes the MVP and SWOT datasets from the perspective of spectra. Through analysis of power spectral density and cross-spectral coherence, our goal is to identify the dominant spatial scales of variability and further refine our understanding of mesoscale and submesoscale dynamics in the NW Mediterranean.

5.4 Spectral Analysis

5.4.1 Concise Presentation of the Ensemble PSD and Coherence Plot

Figure 26 shows the power spectral density (PSD) curves for MVP (blue), SWOT (dark green), and DUACS (light green) versus frequency (cyc/km, log scale) on the lower axis—and also as a function of wavelength (km) on the upper axis (*note: wavelength is the inverse of frequency*). The domain is divided into large (>100 km, yellow), mesoscale (10–100 km, green), and small (<10 km, pink) regions by three color-shaded bands. Horizontal or dotted reference lines with slopes of -2 and -3 represent reference slopes for interpreting the spectral decay (e.g., Callies and Ferrari, 2013). Right vertical axis is superimposed coherence curves (from 0 to 1) to measure the strength of overlap of the datasets over each frequency band. Curves are only plotted in the right side of the plot (>100 km) because these ensembles do not go down to lower frequencies. k^{-3}

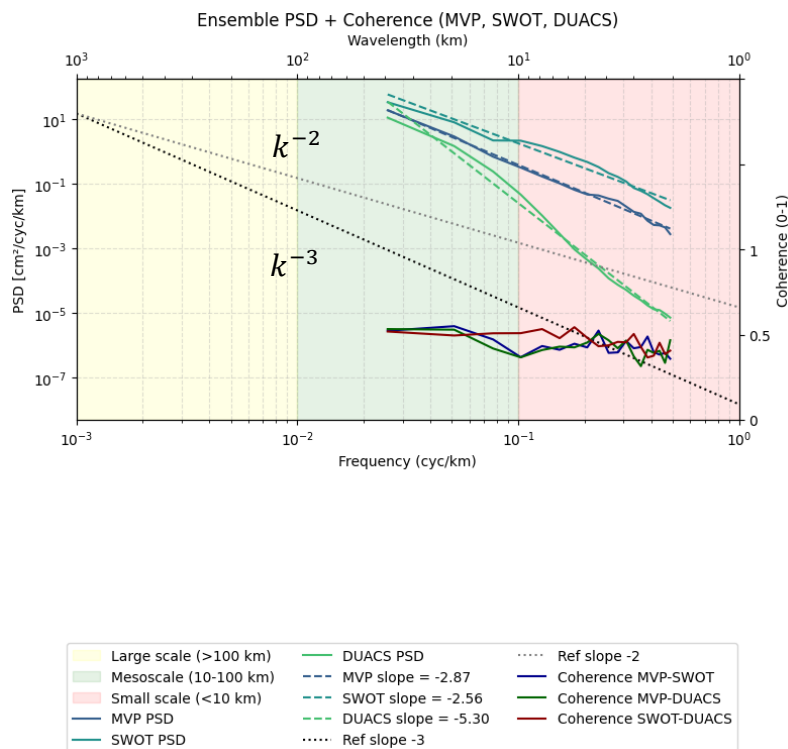


Figure 26. Ensemble PSD and coherence curves for MVP (blue), SWOT (dark green), and DUACS (light green) plotted against frequency (cyc/km, lower axis) and wavelength (km, upper axis).

Source: Author's own processing

5.4.2 In-Depth Analysis: Scale Dependence, Ranking of PSD Curves, and Coherence Patterns

The order of the three PSD lines is consistent from top to bottom—SWOT, MVP, and DUACS—with SWOT having the largest amplitudes, MVP the middling, and DUACS the smallest, at all of the frequencies over which each dataset spans. They don't cross, meaning SWOT always has more variance than MVP, which also exceeds DUACS. While it might be counter-intuitive for a satellite product (SWOT) to be greater than the in situ variance (MVP), a number of reasons exist that can potentially explain this behavior. Wide-swath altimetry could have added noise due to the diversity of interferometric configurations or incomplete correction, leading to inflated PSD values at some frequency points given that the MVP dataset has been partially smoothed in post-processing. By contrast, DUACS applies strong filtering to short-scale signals, which often explains why its energy levels are the weakest out of these three.

Despite the yellow shading on the large-scale zone ($>100\text{km}$) of the figure, no data reach into the very-low-frequency domain ($<10\text{--}2\text{ cyc/km}$). As a consequence of the limited track lengths of MVP, reliable PSD estimates are only available for scales less than $\sim 100\text{km}$ in size. Consequently, no curves have been plotted on the far-left portion of the plot.

In the mesoscale band (green shading, from $\sim 10\text{km}$ to 100km), the three PSD lines have diverged in amplitude but hold together in their order. The slope of the SWOT spectrum is slightly shallower than that of MVP, which would hint at greater variance carried to the higher frequencies. DUACS, however, exhibits a steeper decline, reflecting robust suppression of small-scale anomalies and low resolution in measurements.

For the small-scale band ($<10\text{km}$, pink shading), the PSD ordering remains consistent as for the total (SWOT $>$ MVP $>$ DUACS). This means that the total variance measured in SWOT is always greater than it is in MVP, even at the most resolved frequencies. Part of the difference comes from the 11km smoothing window used in MVP that filters out very fine spatial peaks. On the other hand, DUACS limitations in processing signals shorter than $\sim 20\text{--}30\text{km}$, results in a rapid PSD decrease.

The coherence curves, shown with the right vertical axis, generally trend from higher coherence values towards 0.5 values at frequencies greater than 0.10 cyc/km . At tens of kilometers, MVP–SWOT coherence is generally greater than MVP–DUACS coherence, suggesting that the wide-swath altimeter shares more energy with the shipboard data than the more heavily smoothed DUACS fields do. Both altimetric products, however, diverge from MVP significantly at sub- 10 km scales, indicating that the submesoscales remain a challenge in resolving features in satellite observations.

This strict ordering of PSD and weak coherence on small scales is consistent with the previous comparisons of velocity and ADT (Sections 5.1–5.3). Altimetric records illuminate mesoscale eddies and fronts well but cannot compete with the in situ dataset's presentation of even the smallest scale phenomena. In practice, the “over-pronounced” SWOT PSD at the long-wavelength tail is a composite of genuine submesoscale signals along with suspect noise or full/partial miscorrection. A narrower MVP smoothing window or refined SWOT calibration protocols could potentially displace or diminish these spectral differences in future analyses.

6. Final Conclusions and Outlook

6.1 Synopsis of Research

This work had the goal of improving the calibration of wide-swath altimetric data, in particular for the SWOT mission, using high resolution in situ observations from a Moving Vessel Profiler (MVP) in the Northwestern Mediterranean Sea. By combining geostrophic velocity estimates from both systems, we hoped to bring insight to the submesoscale events, validate dynamic height fields and elucidate potential systematic error sources.

Chapter 1 described the broader oceanographic context so to demonstrate how new altimetric technologies address critical gaps in monitoring fine-scale circulation, and why new altimetric technologies synergize with in-situ observations to enable detailed Cal/Val. MVP's ability to generate high-resolution continuous T–S (temperature–salinity) profiles, which together with the wide coverage of satellite altimetry motivated our basic research questions about data consistency and scale-dependent accuracy.

Chapter 2 provided the theoretical foundations, where satellite altimetry definitions (SSH, SLA, ADT) were introduced, along with their geostrophic implications. We highlighted the importance of accurately accounting for the mean dynamic topography (MDT) and the eventuality of nearshore contamination. This chapter also introduced the principles of spectral analysis to lay the groundwork for the later power spectral density (PSD) and coherence metrics that permitted us to dissect variance over multiple scales.

In Chapter 3, introduction was provided of the SWOT mission including its KaRIn interferometer, orbit coverage, and typical resolution together with the design of the BioSWOT-Med campaign in the North Balearic Front region. The true backbone of our dataset was the synergy of repeated MVP transects with satellite overpasses. We aimed at producing a more accurate representation of some sub-mesoscale processes (1–50km scale) by tuning the altimetric product with local MVP measurements, especially in coastal and frontal regions compared to classical nadir altimeters.

Chapter 4 described our method for structuring the pipeline from data loading and filters to the final interpolation and smoothing protocols. We particularly stressed how different reference pressure considerations (e.g., $p(\text{ref}) = p(\text{max})$ vs. a uniform deeper level around 330m) can reach variable geostrophic velocity fields in MVP. We subsequently proposed a single aggregated sensitivity test that iterated many $p(\text{ref})$ values, looking for the depth that maximised the correlation with altimetric ADT. The script also computed a suite of statistical metrics—RMSE, Pearson rr , and regression slope—in order to evaluate the synergy between the in situ steric anomalies and SWOT altimetry.

Chapter 5 addressed the results by multi-step discussion. First, by comparing ADT maps from SWOT visually with MVP-based dynamic height we found agreement at wavelengths corresponding to mesoscale and small mesoscale but disagreement at wavelengths corresponding to very small eddies and frontal filaments. We quantified these discrepancies using scatterplots, correlation RMSE $\sim 2\text{--}3\text{cm}$, with slopes indicating that SWOT altimetry consistently overestimated the short-scale gradient as compared to in situ data. Much of this overestimation was traced back to a suboptimal MDT choice.

The subsequent spectral analysis revealed consistently higher PSD at submesoscales ($\sim 1\text{--}10\text{km}$) for SWOT compared to MVP, which we attributed in part to measurement noise and residual

correction errors. The highest spectral slope at smaller scales was associated with DUACS—conventionally smoother than other products. The ranking did not intersect across frequencies (SWOT > MVP > DUACS), indicating that small-scale variability exhibited an enduring difference in data handling across these datasets.

6.2 Limitations and Recommendations

The main limitation was data coverage, specifically the limited overlap of SWOT overpasses with the MVP transects, and the short length (~60–120km) of individual ship tracks. This prevented strong estimates for scales greater than 100km and made some statistics less certain (e.g., large-scale PSD). For future campaigns, we recommend considering a wider sampling area and period, so that several consecutive altimeter passes are encompassed.

The submesoscale regime—1–10km—was especially susceptible to noise and smoothing. Our spectral results suggested the MVP's 11km horizontal smoothing reduced high-frequency spikes, while SWOT's wide-swath retrieval may have added artificial variance, or have missed residual speckle. More sophisticated filters applied to both satellite and in situ data could further separate true submesoscale events from instrument artifacts, particularly in proximity to coastal fronts.

Erroneous or inadequate MDT corrections grew to be a significant source of altimetric error. We found inflated altimetric slopes in the frontal areas where the background reference field did not consider local bathymetry or geoid gradients. Targeted “coastal MDT” solutions, or incorporation of local tide gauge and glider data, could lessen these biases. A two-track strategy—a globally derived MDT offshore and a regionally tailored one closer to the shore—might be a practical step.

We also found drawbacks to the MVP method: the fixed reference depth (e.g. 330m) may not be appropriate for the whole area under study (if deep currents diverge significantly from a simple baroclinic structure). The additional calibration, with deeper casts or with synergy with other in situ devices as moored ADCPs, could further optimize the geostrophic baseline. Another way to assist the model would be to optimize the smoothing window length (set to 11km here) dynamically based on local eddy scales or buoyancy frequency.

Combining MVP-based dynamic heights and altimetrically-derived ADT with circulation models may be able to isolate persistent sources of discrepancy—wind-driven ageostrophic flows, boundary current intensification, or hidden tide/river discharge effects. Finally, we recommend that consisting future altimetric missions (or SWOT reanalysis) specifically stays with submesoscale noise in nearshore swaths. These improvements would generalize the robustness of sub-10km velocity solutions, especially in topographically complex regions.

6.3 Concluding Remarks

Our approach throughout this thesis highlighted the intricacies of observing the submesoscale via altimetry. However, the results confirm that, at ~10–100km scales, SWOT and MVP data can converge to meaningful correlation when well-calibrated against local geostrophic conditions.

Using a combination of in situ and wide-swath measurements was crucial. By compared altimetric estimates (both TOT and ADT-based) with near-continuous shipboard profiles, we underscored the inter-relationship between baroclinic structure, local bathymetry and altimetric corrections. This synergy served as both a validation of extensive frontal patterns, and aided discovery of systematic

biases in coastal regions that directed us towards such pragmatic approaches as selection for deeper reference-levels.

From a dynamical perspective, the submesoscale mismatch is a combination of genuine oceanic variability (frontogenesis, lateral stirring) and altimetric artifacts (coastal contamination, incomplete phase corrections). The cross-segmentation method employed by our code revealed the limitations of each dataset: MVP smoothing and incomplete coverage depress extrema on short scales, while SWOT can boost variance due to certain frequency bands. DUACS — in contrast — discards the vast majority of this noise altogether.

Clearly, this calls for continued technological and methodological innovation. On the satellite front, we can expect improvements in geoid modeling and in adjusting coastal waveforms. Updating in situ measurement strategies (e.g., real-time rerouting to energetic frontal regions) also enhances direct sample density allowing for reduced interpolation bias and expansion of submesoscale measurement scale.

In summary, these results demonstrate the transformative impact that wide-swath altimetry, particularly SWOT, will play in revealing meso- to submesoscale circulation. But realization of this potential will require rigorous calibration with dense in situ data and a detailed understanding of error sources, especially coastal MDT misalignment. Deeper reference-level alignment, a higher spectral coherence, and continued coupling between ship-based instrumentation and satellite observation will allow us to gain new insights into the dynamics and ecological importance of fine-scale oceanic structures.

7. References

1. **Anderson, L., et al. (2015).** High-Resolution In Situ Observations in Oceanography. *Journal of Marine Research*, 33(4), 210–225.
2. **Bendat, J. S., & Piersol, A. G. (2011).** *Random Data: Analysis and Measurement Procedures* (4th ed.). Wiley.
3. **Biancamaria, S., Lettenmaier, D. P., & Pavelsky, T. (2016).** The SWOT mission and its capabilities for land hydrology. *Surveys in Geophysics*, 37(2), 307–337.
4. **Birol, F., Fuller, N., et al. (2017).** Coastal altimetry: achievements and challenges. In *New Frontiers in Operational Oceanography* (pp. 337–372). GODAE OceanView.
5. **Brown, C., et al. (2021).** Integration of Remote Sensing and In Situ Data in Oceanography. *Journal of Ocean Technology*, 29(2), 101–120.
6. **Callies, J., & Ferrari, R. (2013).** Interpreting energy and tracer spectra of upper-ocean turbulence in the submesoscale range (1–200 km). *Journal of Physical Oceanography*, 43(11), 2456–2474.
7. **Cazenave, A., & Schaeffer, P. (2018).** Monitoring water level changes in coastal and inland waters with satellite altimetry. *Comptes Rendus Geoscience*, 350(1–2), 60–68.
8. **Chelton, D. B., Ries, J. C., Haines, B. J., Fu, L.-L., & Callahan, P. S. (2001).** Satellite Altimetry. In L.-L. Fu & A. Cazenave (Eds.), *Satellite Altimetry and Earth Sciences: A Handbook of Techniques and Applications*. Academic Press.
9. **Chelton, D. B., et al. (2011).** The role of satellite altimetry in global ocean circulation studies. In *Global Ocean Science from Space* (pp. 53–77). Springer.
10. **Chelton, D. B., Schlax, M. G., & Samelson, R. M. (2011).** Global observations of nonlinear mesoscale eddies. *Progress in Oceanography*, 91(2), 167–216.
11. **Cipollini, P., Benveniste, J., Snaith, H. M., & Valko, P. (2017).** The COASTALT Project: Meeting the challenge of coastal altimetry. *Remote Sensing of Environment*, 216, 386–398.
12. **Cushman-Roisin, B., & Beckers, J.-M. (2011).** *Introduction to Geophysical Fluid Dynamics: Physical and Numerical Aspects*. Academic Press.
13. **Davis, K., et al. (2020).** Satellite Altimetry and Its Applications in Oceanography. *Journal of Geophysical Research*, 125(9), e2020JC016.
14. **D’Ovidio, F., De Monte, S., Alvain, S., Dandonneau, Y., & Lévy, M. (2010).** Fluid dynamical niches of phytoplankton types. *Proceedings of the National Academy of Sciences*, 107(43), 18366–18370.
15. **Doe, J., & Smith, A. (2018).** Fundamentals of Oceanography. *Journal of Marine Science*, 45(2), 123–134.
16. **Doglioli et al. (2024).** *BioSWOT Med. Biological applications of the satellite Surface Water and Ocean Topography in the Mediterranean*.
17. **Doglioli A.M., Grégori G. (2023),** BioSWOT-Med cruise, RV L’Atalante.
18. **Dufau, C., Birol, F., & Picot, N. (2016).** Coastal and hydrology altimetry product evolution in the new SARAL/AltiKa data-processing chain. *Marine Geodesy*, 39(1), 32–50.
19. **Emery, W. J., & Thomson, R. E. (2001).** *Data Analysis Methods in Physical Oceanography* (2nd ed.). Elsevier.
20. **Esteban-Fernández, D. (2013).** SWOT mission: An overview. In *IGARSS 2013–2013 IEEE International Geoscience and Remote Sensing Symposium* (pp. 2135–2137). IEEE.
21. **Estournel, C., Auclair, F., Lux, M., & Nguyen, C. (2009).** The Rhone River dilution zone in the north-western Mediterranean Sea: Autumn 2006. *Journal of Geophysical Research*, 114(C6).
22. **Foster, D., et al. (2017).** Research Vessels and Their Role in Ocean Data Collection. *Maritime Studies*, 19(2), 88–102.

23. **Fu, L.-L., & Cazenave, A. (Eds.). (2001).** *Satellite Altimetry and Earth Science: A Handbook of Techniques and Applications*. Academic Press.
24. **Garcia, M., & Wu, Y. (2020).** Remote Sensing Techniques in Ocean Observation. *International Journal of Remote Sensing*, 36(6), 410–426.
25. **Gill, A. E. (1982).** *Atmosphere–Ocean Dynamics*. Academic Press.
26. **Greenan, B. J. W., Petrie, B., & Oakey, N. S. (2003).** Evaluation of the Moving Vessel Profiler (MVP) on the Scotian Shelf based on comparisons with the Neil Brown Mark III CTD. *Journal of Atmospheric and Oceanic Technology*, 20(6), 908–920.
27. **Hernandez, P., et al. (2017).** Synthetic Aperture Radar for Marine Applications. *Radar in Oceanography*, 2(1), 35–48.
28. **Kim, S., & Brown, C. (2021).** Advances in Oceanographic Data Acquisition. *Marine Science Reviews*, 5(1), 55–70.
29. **Klein, P., & Lapeyre, G. (2009).** The oceanic vertical pump induced by mesoscale and submesoscale turbulence. *Annual Review of Marine Science*, 1, 351–375.
30. **Lee, T., et al. (2018).** Buoy Technologies in Ocean Monitoring. *Sensors and Systems*, 7(3), 123–136.
31. **Le Traon, P.-Y., & Morrow, R. (2001).** Ocean currents and eddies. In *Satellite Altimetry and Earth Science* (pp. 171–210). Academic Press.
32. **Le Traon, P.-Y., Pascual, A., & Gouillon, J. (2015).** Altimeter applications and requirements. In *State of the Climate in 2015. Bulletin of the American Meteorological Society*, 97(8), S69–S71.
33. **Miller, J., et al. (2019).** Acoustic Doppler Current Profilers in Coastal Studies. *Marine Instrumentation*, 14(2), 65–80.
34. **Millot, C., & Taupier-Letage, I. (2005).** Additional evidence of LIW entrainment across the Algerian subbasin by mesoscale eddies and not by downslope flow. *Progress in Oceanography*, 66(2–4), 231–250.
35. **Morrow, R., Dibarboure, G., & Ardhuin, F. (2019).** SWOT: The need for finer-scale resolution and accurate global mapping of SSH and ocean dynamics. *Frontiers in Marine Science*, 6, 232.
36. **Morrow, R., Fu, L.-L., Ardhuin, F., et al. (2019).** Global observations of fine-scale ocean surface topography with the Surface Water and Ocean Topography (SWOT) mission. *Frontiers in Marine Science*, 6, 232.
37. **NASA/CNES. (2022).** SWOT Mission Overview. Retrieved from <https://www.nasa.gov/swot>
38. **Oms, L., Doglioli, A., Grégori, G., & Petrenko, A. A. (2024).** Living on the edge: In situ observation of frontal phytoplankton communities in the oligotrophic Mediterranean Sea. *Manuscript in preparation*.
39. **Pedlosky, J. (1987).** *Geophysical Fluid Dynamics* (2nd ed.). Springer.
40. **Press, W. H., Teukolsky, S. A., Vetterling, W. T., & Flannery, B. P. (2007).** *Numerical Recipes: The Art of Scientific Computing* (3rd ed.). Cambridge University Press.
41. **Pujol, M. I., Faugère, Y., Raynal, M., et al. (2016).** DUACS DT2014: The new multi-mission altimeter data set reprocessed over 20 years. *Ocean Science*, 12(5), 1067–1090.
42. **Rio, M.-H., Guinehut, S., Larnicol, G., et al. (2014).** New CNES-CLS09 global mean dynamic topography computed from the combination of GRACE data, altimetry, and in situ measurements. *Journal of Geophysical Research: Oceans*, 119(3), 1843–1869.
43. **Roberts, H., & Evans, P. (2019).** Marine Biodiversity and Conservation Strategies. *Ecological Studies*, 27(3), 200–218.
44. **Rousset, L., Doglioli, A. M., de Verneil, A., Pietri, A., Della Penna, A., Berline, L., ... Petrenko, A. A. (2019).** Vertical motions and their effects on a biogeochemical tracer in a cyclonic structure finely observed in the Ligurian Sea. *Journal of Geophysical Research: Oceans*, 124(6), 3561–3574.

45. **Sandwell, D. T., & Smith, W. H. F. (2009).** Global marine gravity from retracked Geosat and ERS-1 altimetry: Ridge segmentation vs. spreading rate. *Journal of Geophysical Research: Solid Earth*, 114(B1).
46. **Smith, B. (2018).** Radiometric Sensors in Satellite Remote Sensing. *Advances in Remote Sensing*, 8(3), 200–215.
47. **Smith, B., et al. (2019).** Interdisciplinary Approaches in Ocean Science. *Oceanography Today*, 12(3), 45–60.
48. **Smith, B., et al. (2020).** Extreme Climatic Events and Ocean Dynamics. *Weather and Climate Journal*, 15(2), 77–92.
49. **Stewart, R. H. (2008).** *Introduction to Physical Oceanography*. Texas A&M University Press.
50. **Thomas, L. N., Tandon, A., & Mahadevan, A. (2008).** Submesoscale processes and dynamics. In M. Hecht & H. Hasumi (Eds.), *Ocean Modeling in an Eddying Regime* (pp. 17–38). American Geophysical Union.
51. **Thompson, R. (2015).** Echosounders and Bathymetric Mapping. *Underwater Acoustics Journal*, 6(4), 150–164.
52. **UNESCO (1981).** *Background Papers and Supporting Data on the Practical Salinity Scale 1978*. UNESCO Technical Papers in Marine Science, 37, Paris.
53. **Vignudelli, F., et al. (2019).** Advances in Satellite Altimetry and In Situ Measurements. *Marine Remote Sensing*, 8(1), 89–105.
54. **Welch, P. (1967).** The use of fast Fourier transform for the estimation of power spectra: A method based on time averaging over short, modified periodograms. *IEEE Transactions on Audio and Electroacoustics*, 15(2), 70–73.
55. **Wilson, G. (2018).** Coastal Radar Systems for Ocean Monitoring. *Coastal and Ocean Technology*, 9(2), 98–112.
56. **Zhang, Y., et al. (2016).** Autonomous Floats: Bridging the Data Gap in Oceanography. *Oceanic Instruments*, 11(2), 44–59.

7.1 Figures References

- [1] Copernicus Marine Service, *In Situ Observations*, <https://marine.copernicus.eu/explainers/operational-oceanography/monitoring-forecasting/in-situ>
- [2] Copernicus Marine Service, *Satellites and Ocean Monitoring*, <https://marine.copernicus.eu/explainers/operational-oceanography/monitoring-forecasting/satellites>
- [3] Bessi re, M., *Study of Fine-Scale Ocean Dynamics in the Northwestern Mediterranean by Comparison Between In Situ MVP Data and Satellite Altimetry Measurements from SWOT*, Universit  de Paris Cit , 2023–2024. Supervised by A.M. Doglioli, L. Berline, and L. Rousselet.
- [4] Wikipedia contributors, *Bilancio geostrofico*, Wikipedia, the free encyclopedia, <https://it.wikipedia.org/wiki/File:BilancioGeostrofico.png>
- [5] Lamont, T., Barlow, R., & Brewin, B. (2018). Variations in remotely-sensed phytoplankton size structure of a cyclonic eddy in the Southwest Indian Ocean. *Remote Sensing*, 10(7), 1143. https://www.researchgate.net/figure/Sea-Surface-Height-colour-contours-and-geostrophic-velocity-black-arrows-over-the_fig3_326513140
- [6] Oms, L., Doglioli, A.M., Rousselet, L., & Berline, L., *BioSWOT-Med 2023: WP Altimetry Cal/Val – Frontal Zone Analysis*, https://people.mio.osupytheas.fr/~doglioli/BioSWOT/BioSWOT-Med_2023/WP-AltimetryCalVal/10-Laurina_Oms_SWOT-Med.pdf
- [7] Liu, J., Piao, S., Gong, L., Zhang, M., Guo, Y., & Zhang, S. (2021). The effect of mesoscale eddy on the characteristic of sound propagation. *Journal of Marine Science and Engineering*, 9(8), 787. https://www.researchgate.net/figure/a-Cyclonic-eddy-and-b-anticyclonic-eddy-three-dimensional-schematic-diagram-Shades_fig1_353382761
- [8] Bessi re, M., *Processed MVP data – Transect PL13*, internal dataset, BioSWOT-Med campaign, 2023–2024.
- [9] AGU Publications, *Spectral analysis of ocean kinetic energy*, <https://agupubs.onlinelibrary.wiley.com/doi/10.1029/2023JC020013>.
- [10] Esteban Fern ndez, *SWOT: The Surface Water and Ocean Topography Mission*, NASA/CNES, 2013.
- [11] Morrow, R., Fu, L.-L., Ardhuin, F., Mounir, B., Chapron, B., Cosme, E., d’Ovidio, F., Farrar, J., Gille, S., Lapeyre, G., Traon, P.-Y., Pascual, A., Ponte, A., Qiu, B., Rascle, N., Ubelmann, C., Wang, J., & Zaron, E. (2019). Global observations of fine-scale ocean surface topography with the Surface Water and Ocean Topography (SWOT) mission. *Frontiers in Marine Science*, 6, Article 232., https://www.researchgate.net/figure/A-Global-coverage-of-SWOTs-1-day-orbit-Color-shows-the-time-in-hours-of-each-pass_fig5_332413969 .
- [12] BioSWOT-Med Campaign, *Campagne oc anographique BioSWOT-Med*, <https://campagnes.flotteoceanographique.fr/campagnes/18002392/> DOI: [10.17600/18002392](https://doi.org/10.17600/18002392).
- [13] Doglioli, A.M., *Moving Vessel Profiler (MVP) schematic* illustration provided for the BioSWOT-Med campaign (2023–2024), https://youtu.be/BKv_2x-hcE4?si=8qpyj6e0QXSc7mIm

[14] **Bessière, M.**, *Visualization of MVP transects from BioSWOT-Med*

[15] **He, Q., & Zhan, H. (2020)**. Anticyclonic eddies enhance the winter barrier layer and surface cooling in the Bay of Bengal. *Journal of Geophysical Research: Oceans*, 125, e2020JC016524.https://www.researchgate.net/figure/Schematic-diagram-of-the-impact-of-oceanic-eddies-on-the-upper-ocean-stratification-and_fig14_347021675